Role of the Cu-Deficient Interface in $Cu(In, Ga)Se_2$ Thin-Film Photovoltaics with Alkali-Metal Doping

Shogo Ishizuka[1,*] and Paul J. Fons[2]

[1] *Research Institute for Energy Conservation, National Institute of Advanced Industrial Science and Technology, Tsukuba, Ibaraki 305-8568, Japan*

[2] *Department of Electronics and Electrical Engineering, Keio University, 4-1-1 Hiyoshi, Kohoku-ku, Yokohama, Kanagawa 223-8521, Japan*

(Received 8 January 2021; revised 18 February 2021; accepted 12 April 2021; published 4 May 2021)

Cu-deficient phases of chalcopyrite $Cu(In, Ga)Se_2$ (CIGS), such as $Cu(In, Ga)_3Se_5$ and $Cu(In, Ga)_5Se_8$, which are occasionally referred to as ordered vacancy compounds and often unintentionally form on CIGS film surfaces and at grain boundaries, are among the most important subjects in developing chalcopyrite thin-film energy-conversion materials and devices. Here, we revisit the role of the Cu-deficient surface layer (CDL) present at the *p*-CIGS/*n*-CdS interface in photovoltaic devices with the effects of alkali-metal doping. The device structure used is alkali-containing soda-lime glass or alkali-free zirconia substrate/Mo/CIGS/$CuInSe_2$-based CDL/CdS/intrinsic and Al-doped ZnO. The photovoltaic device performance deteriorates with increasing CDL thickness when no alkali metal is added. However, the CDL thickness significantly affects the results of alkali-halide RbF postdeposition treatment (PDT) and the use of a thick CDL enhances the beneficial effects of RbF PDT, resulting in photovoltaic performance enhancements manifested by improvements in the open-circuit voltage and fill-factor values. On the other hand, RbF PDT leads to degradation of the device performance when the CDL is thin. High Rb concentration and significant Ga diffusion from the CIGS layer to the surface CDL with RbF PDT are observed when the CDL is thick. The formation of metastable acceptors, namely, an increase in the nominal carrier density in CIGS, is observed with light-soaking (LS) treatments, regardless of the thickness of CDL. Nevertheless, improvements in photovoltaic efficiency with LS treatments are observed only from devices grown with a thick CDL.

DOI: 10.1103/PhysRevApplied.15.054005

I. INTRODUCTION

Chalcogenide energy-conversion devices represented by chalcopyrite $Cu(In, Ga)Se_2$ (CIGS) solar cells have the advantages of high energy-conversion efficiency, cost-effectiveness, the capability of flexible and lightweight device fabrication, and durability [1–3]. In addition, thermoelectric conversion devices [4–7] and photocathodes for photoelectrochemical water-splitting hydrogen evolution [8–15] are among a wide variety of possible applications of chalcogenide materials. Cu-deficient phases of CIGS, which are occasionally referred to as ordered vacancy compounds (OVCs), often unintentionally form on CIGS film surfaces and at grain boundaries, are recognized as important subjects in developing photovoltaic energy-conversion materials and devices [16–26]. It has also been reported in the literature that photocathodes for water-splitting hydrogen evolution, consisting of a Cu-deficient $CuGa_3Se_5$ film, demonstrate better performance than those fabricated with conventional $CuGaSe_2$ electrodes [14]. As such, the importance of a detailed understanding of the material properties, potential for further developments, and controllability of Cu-deficient phases are increasing.

Cu-deficient phases of CIGS have long been a focus of attention and have been well-studied to date. A report on a CIGS solar cell in 1974 was based on the *p*-$CuInSe_2$/*n*-CdS heterojunction [27]. Two decades later, a model for the formation of a *p*-*n* junction based on the *p*-$CuInSe_2$/*n*-OVC heterojunction, the so-called "buried *p*-*n* junction" was proposed [16] and the material properties of Cu-deficient phases attracted attention. To date, there have been many studies carried out on Cu-deficient CIGS phases, in terms of material properties, as characterized by theoretical calculations [28], x-ray diffraction (XRD) [17], and Raman spectroscopy [18–20,24]. Additional studies have focused on other structural, optical, and electrical properties, including energy-band alignment of the device structure [28–31].

Nevertheless, most studies reported, to date, have been carried out independently of the effects of alkali-metal

*shogo-ishizuka@aist.go.jp

doping. For the last several years, CIGS photovoltaic efficiencies have been improved with alkali-metal doping, mainly using postdeposition treatment (PDT) techniques with alkali halides, such as KF, RbF, and CsF [32–34]. It has been reported that alkali-halide PDT modifies CIGS surface properties, such as morphology and the energy-band structure [35–39]. It has also been suggested that there is a strong correlation between the effects of PDT and CIGS surface conditions (near stoichiometric or Cu-deficient) [40], implying that an understanding of the role of a Cu-deficient surface layer (CDL) present in CIGS photovoltaic devices in conjunction with alkali-metal effects is an important subject.

Here, we revisit the role and effects of the CDL present at the CIGS/CdS interface in photovoltaic devices. $CuInSe_2$-based CDLs, which consist of mixed phases of chalcopyrite I-III-VI_2 and OVCs such as I-III_3-VI_5 (I, Cu; III, In, Ga; VI, Se), are intentionally formed on CIGS film surfaces with various thicknesses and alkali-metal doping conditions. The effects of the presence of a CDL at the CIGS/CdS interface on alkali-metal effects, metastable acceptor formation, and consequent photovoltaic device properties are particularly focused upon.

II. EXPERIMENT

Polycrystalline thin films of CIGS are grown on sputtered Mo-coated (800 nm in thickness) alkali-containing soda-lime glass (SLG) and alkali-free sintered zirconia substrates by a three-stage coevaporation process [41] using elemental Cu, In, Ga, and Se Knudsen cell sources in a vacuum chamber. Elemental In, Ga, and Se are supplied during the first stage at a substrate temperature (T_s) of 350 °C. Elemental Cu and Se are supplied during the second stage and elemental In and Se are successively supplied during the third stage at $T_s \approx 540$ °C. Thus, the surface [Ga]/([Ga] + [In]) (GGI) composition ratio is lower than that in the film, and the structure of the conduction-band minimum (E_C) of CIGS films used in this study is single graded. The band-gap energies (E_g) for $CuInSe_2$, $CuIn_3Se_5$, $CuGaSe_2$, and $CuGa_3Se_5$ are assumed to be approximately 1.0, 1.2, 1.7, and 1.85 eV, respectively [30]. There are two reasons for the use of such low GGI surface films. One is for the examination of the effects of RbF PDT using $CuInSe_2$-based film surfaces. In our previous report, the beneficial effects of RbF PDT on $CuGaSe_2$ photovoltaic performance were small, and thus, elemental In was found to be key in optimizing the beneficial effects of RbF PDT in improving the device performance [42]. In other words, the presence of Ga in the surface region may obscure the effects of heavy-alkali-metal halide PDT. Also, the formation of the $RbInSe_2$ phase is observed for $CuInSe_2$ and CIGS films with RbF PDT, whereas such distinguishable alkali-metal-related phase formation is not observed on $CuGaSe_2$ surfaces with RbF PDT [43], although different experimental conditions, such as the use of different T_s values, may lead to different results. The detailed roles of the alkali-metal-related phases are still open to discussion because enhanced device performance can be obtained with heavy-alkali-metal halide PDTs, regardless of the formation of the phases [44]. The other reason for the use of a single GGI gradient is that this profile follows that of the $Cu(In, Ga)(Se, S)_2$ photoabsorber layers employed in record efficiency devices and practical or commercial CIGS solar modules [45,46], except for the presence of sulfur, which modifies the structure of the valence-band maximum (E_V), resulting in a reduction of carrier recombination near the p-n junction region [45,47]. Thus, although the effect of the lack of elemental S should be considered, the insights obtained in this study are expected to contribute to developments in industry and to the understanding of the underlying physics.

After CIGS film growth, CdS buffer layers are deposited by chemical-bath deposition (CBD) using an aqueous solution consisting of 12 ml $CdSO_4$ solution ($CdSO_4 \cdot 8/3H_2O$, 3.84 g; H_2O, 1000 ml), 6 ml NH_2CSNH_2 solution (NH_2CSNH_2, 120 g; H_2O, 1000 ml), 32 ml ammonia solution (NH_4OH, 28%), and 180 ml H_2O at 80 °C for 16 min to obtain a 50-nm-thick CdS layer. The device structure is SLG or zirconia substrate/Mo/CIGS/$CuInSe_2$-based CDL/CdS/intrinsic ZnO (i-ZnO)/Al-doped ZnO (ZnO:Al). The ZnO layers are deposited by sputtering. The thickness of the CdS layer used for all CIGS devices is 50 nm. The thicknesses of i-ZnO and ZnO : Al layers are approximately 50 and 300 nm, respectively. Ni-Al grid electrodes are deposited onto the ZnO : Al surface to measure the photovoltaic properties.

Unlike the case of ternary $CuGaSe_2$ films [48], the CIGS/CDL interface in films used in this study is unclear. To be accurate, therefore, the term Cu-*deficient region* may be more appropriate to express the CIGS surface conditions than the term Cu-*deficient layer*. However, the term CDL is often used to indicate the Cu-deficient surface region in the literature [21,22]. Thus, hereafter, the term CDL is used. The thickness of the CDLs is controlled by varying the duration of the third stage, as described in the next section (Sec. III A). Four types of CIGS films, namely, CIGS types A, B, C, and D, are prepared, where type A possesses the thinnest CDL and type D possesses the thickest. As a consequence, the total thickness of the CIGS/CDL film varies from approximately 2.0 μm (type A) to 2.4 μm (type D).

RbF PDT is performed on CIGS/CDL films using Knudsen cell sources at a substrate temperature T_s of 350 °C. The Knudsen cell source temperature of the RbF source (T_{RbF}) used is 570 or 590 °C. The duration of PDT in this study is 10 min. The CIGS-film-growth sequence is shown in Fig. 1, where t_{3rd} and t_{STP} are the duration of the third stage and the time from the beginning of the third stage to the stoichiometry point

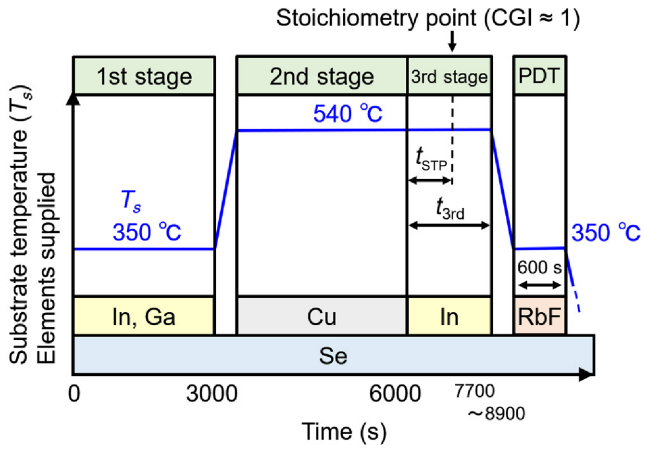

FIG. 1. CIGS film growth sequence used in this study. Time axis is not to scale.

determined with pyrometer profiles [49], respectively. The stoichiometry point is the time when [Cu]/([Ga] + [In]) (CGI) becomes unity with increasing In content during the third stage. The CIGS/CDL films and devices are characterized using scanning electron microscopy (SEM) equipped with an electron-beam-induced current (EBIC) system, secondary-ion mass spectrometry (SIMS), electron-probe microanalyzer (EPMA), XRD, photoluminescence (PL), capacitance-voltage (*C-V*), and current-voltage (*I-V*) measurements. The solar-cell device area is 0.52 cm^2. SIMS measurements are carried out using Cs^+ (5.0 kV, 54×54 μm^2) as the primary ion. XRD measurements are carried out in θ-2θ mode using Cu $K\alpha$ radiation. PL and time-resolved PL (TRPL) measurements are carried out using the sample structure of substrate/Mo/CIGS/CDL/CdS (without ZnO layers) at room temperature (approximately 25 °C) with an excitation light source of 532 nm, 0.31 mW (PL), and 0.11 mW (TRPL), and a spot size of approximately 1 mm^2. Nominal carrier density (N_{CV}) profiles calculated from *C-V* measurement results are obtained at room temperature (approximately 25 °C) using a 100 kHz ac signal, and a dielectric constant value $\varepsilon_{CIGS} \approx 13.5\varepsilon_0$ are used for analysis, where ε_0 is the dielectric constant of vacuum. Solar-cell parameters, namely, the photovoltaic efficiency, open-circuit voltage (V_{OC}), short-circuit current density (J_{SC}), and fill factor (FF), are measured at 25 °C under AM1.5G (100 mW/cm^2) illumination. No antireflection coating is used in this study. Light-soaking (LS) treatments are performed on open-circuit CIGS solar cells under 1 sun illumination at 90 °C under vacuum for 3 h to examine the formation of metastable acceptors [50]. In Sec. III, CIGS sample details (without RbF PDT) are explained in Sec. III A, the effects of RbF PDT with various CDL thicknesses are discussed in Sec. III B, and additional information regarding metastable acceptor formation with LS treatment is discussed in Sec. III C.

III. RESULTS AND DISCUSSION

A. CIGS/CDL film properties

The properties of CIGS films and devices grown without (w/o) PDT are shown to specify the premise of experimental conditions used in this study. The CGI and GGI values obtained from CIGS type *A*, *B*, *C*, and *D* films are shown in Table I. Here, the duration of the third stage, t_{3rd}, is determined as

$$t_{3rd} = t_{STP}a,$$

where *a* is 1.05, 1.25, 1.65, and 2.00 for CIGS types *A*, *B*, *C*, and *D*, respectively.

Solar-cell parameter variations observed from CIGS type *A*, *B*, *C*, and *D* devices fabricated using alkali-containing SLG and alkali-free zirconia substrates without RbF PDT are shown in Figs. 2(a) and 2(b). Notably, LS treatments are not performed in Secs. III A and III B. LS treatments are performed in only Sec. III C. It is found that photovoltaic efficiencies decrease with increasing CDL thickness due to decreases in the values of V_{OC} and FF, regardless of the substrate material. This trend is

TABLE I. CGI and GGI values calculated from the elemental compositions obtained by EPMA measurements using acceleration voltages (V_{acc}) of 5 and 15 kV, which correspond to approximate effective depths of 0.1 and 1.0 μm from the CIGS/CDL film surface [51], respectively.

CIGS type	Substrate	*a*	CGI @$V_{acc} \approx 5$ kV	CGI @$V_{acc} \approx 15$ kV	GGI @$V_{acc} \approx 5$ kV	GGI @$V_{acc} \approx 15$ kV
A	SLG	1.05	0.84	1.02	0.026	0.065
B	SLG	1.25	0.71	0.96	0.013	0.051
C	SLG	1.65	0.55	0.81	0.0085	0.033
D	SLG	2.00	0.58	0.74	0.0065	0.023
A	Zirconia	1.05	0.85	0.99	0.029	0.12
B	Zirconia	1.25	0.81	0.96	0.019	0.11
C	Zirconia	1.65	0.74	0.87	0.012	0.070
D	Zirconia	2.00	0.66	0.78	0.0095	0.042

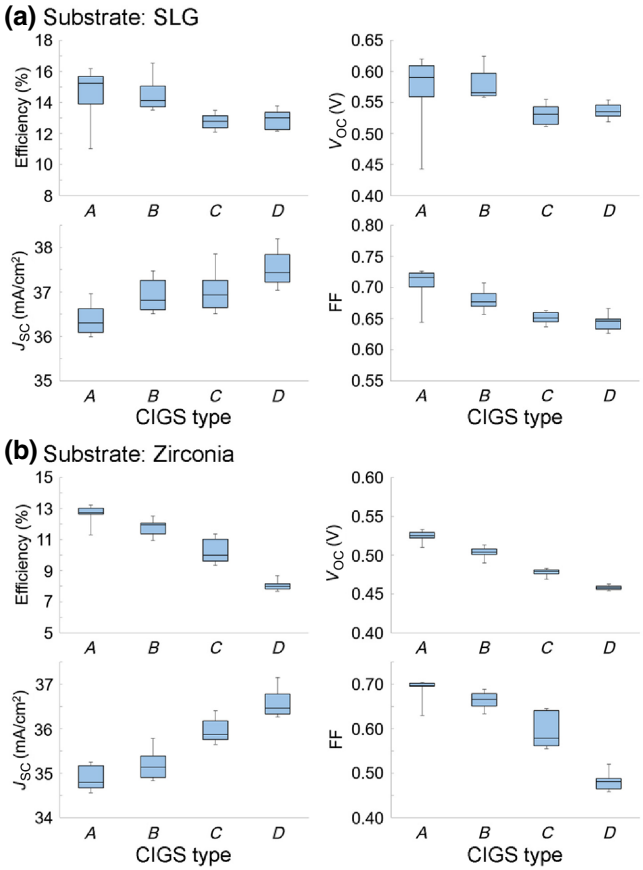

FIG. 2. Solar-cell parameter variations obtained from CIGS type *A*, *B*, *C*, and *D* devices grown on alkali-containing SLG (a) and alkali-free zirconia (b) substrates (w/o RbF PDT).

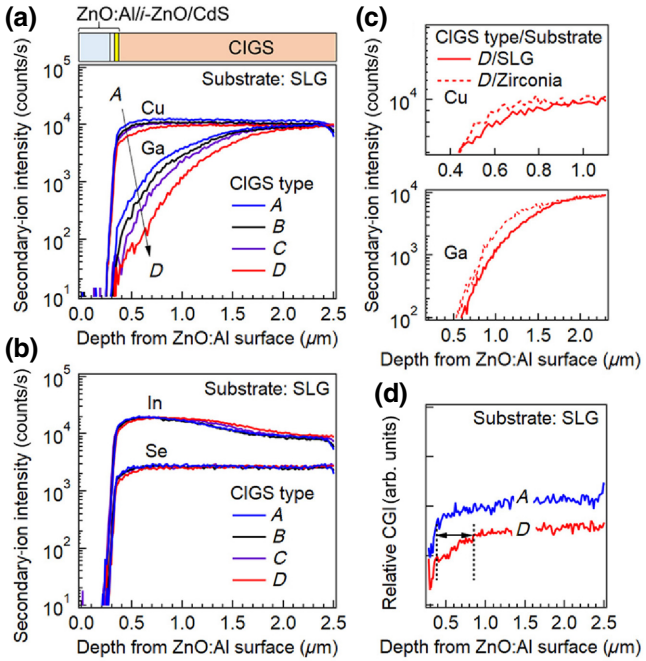

FIG. 3. Elemental Cu and Ga (a) and In and Se (b) SIMS depth profiles obtained from CIGS films grown on SLG substrates. (c) Comparison of elemental Cu and Ga diffusion to the surface region in CIGS type *D* films grown on alkali-containing SLG and alkali-free zirconia substrates. (d) Comparison of CGI depth profiles in CIGS type *A* and *D* films grown on SLG substrates.

the same as the results observed from conventional double-graded GGI profile CIGS devices [22,26,40], although a very thin (∼10 nm) CDL may be effective in increasing V_{OC} [26,40]. A decrease in J_{SC} with increasing CDL thickness is observed from double-graded GGI devices in the literature [22,26,40]. In this study, however, a significant increase in J_{SC} with increasing t_{3rd}, namely, with increasing CDL thickness, is observed from single-graded GGI devices. This result is attributable to the lack of a high GGI region at the CIGS/CDL film surface, as shown in Figs. 3(a) and 3(b). The decrease of GGI from CIGS type *A* to *D* is expected to lead to smaller band-gap energies, resulting in high J_{SC} values.

Elemental Ga and Cu, which are supplied during the first and second stages, respectively, are more likely to migrate and diffuse to the surface in alkali-free films than in alkali-containing films. This trend is shown in Fig. 3(c) and Table I. Also, the GGI values of the surface region ($@V_{acc} \approx 5$ kV) of all films are less than 0.03, indicating that the presence of elemental Ga is almost negligible. The thickness of the CDL in CIGS type *A* films is very thin, whereas CIGS type *D* films grown on SLG substrates possess the thickest CDL of approximately 0.5 μm, as shown in Fig. 3(d). The thicknesses of the CDLs in CIGS type *B* and *C* films may assume intermediate values based upon data given in Table I and Fig. 3(a). Surface and cross-section SEM images for CIGS type *A*, *B*, *C*, and *D* films grown on SLG and zirconia substrates are shown in Figs. 4(a) and 4(b). These top views are misleading, as CIGS films grown on SLG substrates consist of larger grains than those of films grown on zirconia substrates. In fact, cross-section SEM images indicate that alkali-free CIGS films have relatively large grain sizes, and no small-grain-size regions are observed in the Mo layer of the films. These grain size trends are consistent with previous reports [51–53]. No significant morphological variations are observed from CIGS type *A*-*D* film surfaces with increasing CDL thickness.

Variations in CIGS 220/204 XRD peaks observed from these CIGS/CDL films in the 2θ range of 44°–46° are shown in Figs. 5(a) and 5(b). The XRD peak splitting observed is more prominent on SLG substrates than that on zirconia substrates and can be attributed to elemental-migration interference effects due to the presence of alkali metals during film growth [52,54], as can be seen in Fig. 3(c). For example, the full width at half maximum (FWHM) values of CIGS 220/204 XRD peaks of CIGS type *D* films grown on SLG and zirconia substrates are

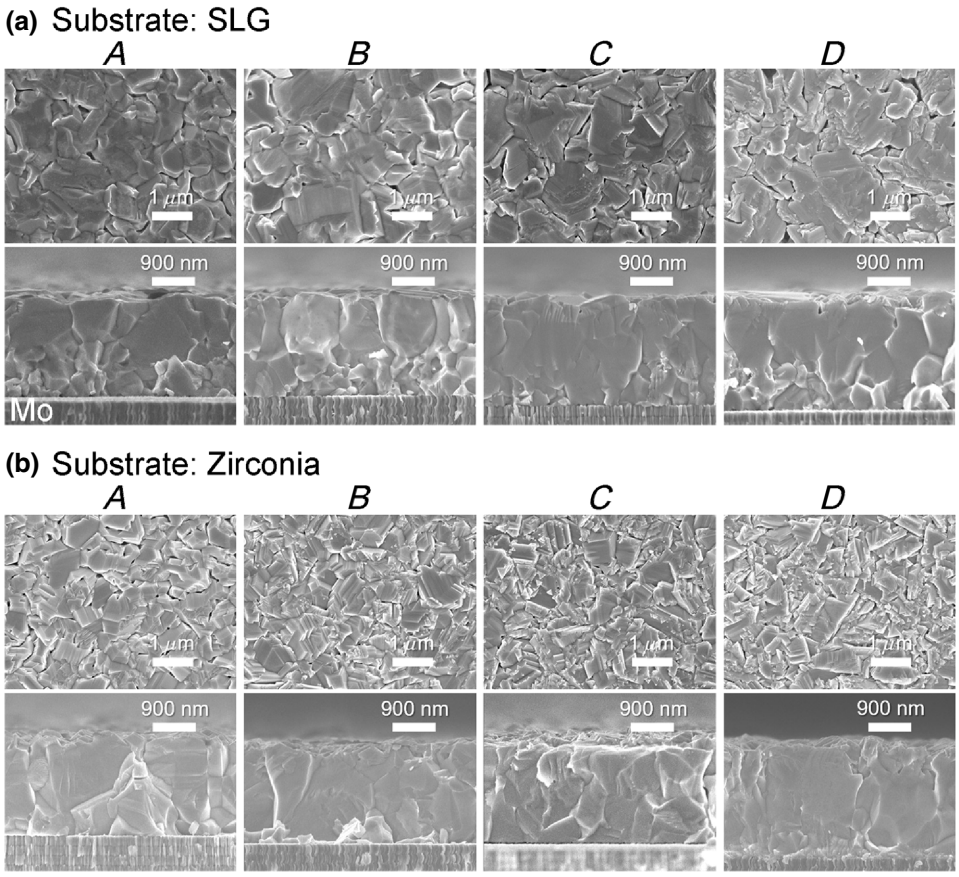

FIG. 4. Surface and cross-section SEM images for CIGS type *A*, *B*, *C*, and *D* films grown on SLG (a) and zirconia (b) substrates.

3960 and 3240 arcsec, respectively. Such an XRD peak separation is often observed in CIGS films that have steep GGI gradient profiles [55,56]. Variations in the XRD peak intensities, namely, an increase in the intensity at around 44.3° and a decrease in intensity at around 45.1° observed with increasing CDL thickness from CIGS types *A* to *D*, shown in Fig. 5(a), correspond to a decrease in GGI values, which can be recognized from the Ga and In profiles shown in Figs. 3(a) and 3(b). Furthermore, it is observed that the XRD peak positions shift to high 2θ angles with a variation of CIGS type from *A* to *D*, implying that the I-III_3-VI_5 phase composition (CDL formation) is enhanced with increasing t_{3rd} [57].

Figures 6(a) and 6(b) show EBIC and SEM and EBIC line-scan profile and SEM images obtained from CIGS type *A* and *D* devices grown on SLG and zirconia substrates. It is reported that the EBIC peak position is likely to deviate from the CDL/CdS interface towards the Mo side with increasing CDL thickness [22]. A similar trend is observed for these devices, although a buried *p*-*n* junction is observed, even in type *A* devices. Also, CIGS type *D* devices show widened depletion layer widths in comparison with those observed in type *A* devices. Here, the depletion layer width, *W*, is generally expressed as

$$W = \varepsilon_{CGS}\varepsilon_0 S/C, \tag{1}$$

where ε_{CIGS}, ε_0, *S*, and *C* are the dielectric constant of CIGS, dielectric constant of vacuum, device area, and capacitance, respectively. When the electron-carrier density at the *n* side (CDL/CdS) increases, the capacitance, *C*, decreases, even if the hole-carrier density at the *p* side (CIGS) is constant and an increase of *W* at the *p* side is expected [58]. Thus, the increased *W* observed in CIGS type *D* devices is attributable to an increase in the effective donor density at the *n* side and an increase of the CDL thickness. This result corresponds to the enhanced Cu deficiency in type *D* films, which is expected to lead to donor-type III_{Cu} defect formation in the CDL.

Figures 6(c) and 6(d) compare elemental Cd depth profiles in CIGS type *A*-*D* films grown on SLG and zirconia substrates. Cd diffusion is suggested to be an important factor in the formation of a buried *p*-*n* junction in the CIGS-film-surface region [59–61]. It is found that there is no significant variation in the Cd depth profiles, except for the type *D* film grown on a SLG substrate, which has the thickest CDL. In Sec. III B, the effects of RbF PDT are examined using these CIGS type *A*-*D* films and devices. It is also found that RbF PDT, which often modifies the CIGS-film-surface morphology and results in the formation of Rb-related secondary phases, has no significant effect on the Cd depth profiles, at least on a submicron scale, as shown in Fig. 6(e).

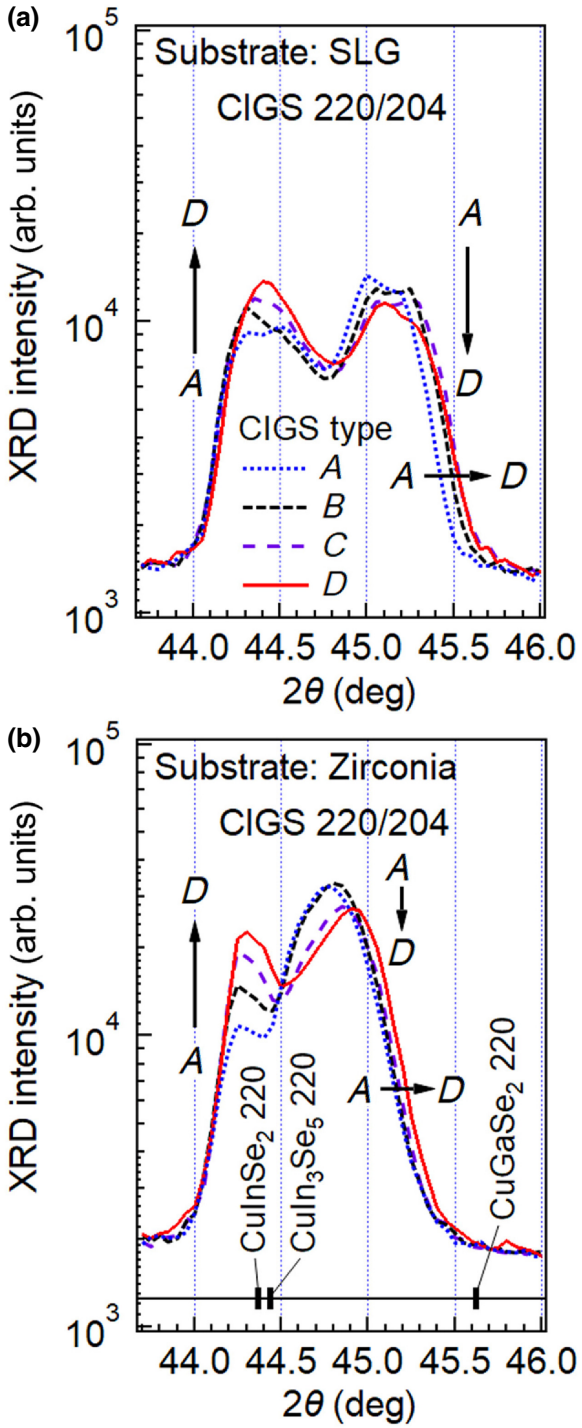

FIG. 5. XRD patterns of CIGS type *A*, *B*, *C*, and *D* films grown on SLG (a) and zirconia (b) substrates obtained at a 2θ value of around 45°. PDF Cards No. 00-023-0209 ($CuInSe_2$), No. 0051-1221 ($CuIn_3Se_5$), and No. 00-035-1100 ($CuGaSe_2$) are referenced.

B. Effects of RbF PDT

To date, numerous reports on the effects of alkali-halide PDT on CIGS films and devices can be found in the literature [1,32–34,52,62]. Although alkali-halide PDT is a promising technique to boost the CIGS photovoltaic performance, the results obtained in different laboratories often depend on experimental conditions, and thus, not only beneficial effects, but also detrimental effects are occasionally observed. Lepetit *et al.* report the deterioration of the CIGS photovoltaic performance with KF PDT, when an OVC phase is absent prior to PDT [40], suggesting that the presence of Cu-deficient phases in the CIGS-film-surface region is necessary to obtain beneficial effects for PDT. On the other hand, Kodalle *et al.* report that RbF PDT leads to improvements in V_{OC}, FF, and concomitant efficiency enhancements when high-Cu-content (CGI ≈ 0.95) CIGS photoaborber layers are used, whereas the photovoltaic performance is found to degrade with RbF PDT for low-Cu-content CIGS (CGI ≤ 0.8) photoabsorber layers [63].

Figure 7 shows variations in solar-cell parameters with RbF PDT obtained from CIGS type *A*-*D* devices grown on SLG substrates. Elemental Rb concentration and depth profiles in corresponding CIGS type *A* and *D* films ($T_{RbF} \approx 570$ °C) and type *B* and *C* films ($T_{RbF} \approx 590$ °C) are shown in Figs. 8(a) and 8(b), respectively. The photovoltaic performance of CIGS type *B* devices improves with a relatively small amount of RbF PDT ($T_{RbF} \approx 570$ °C), whereas it degrades with a large amount of RbF PDT ($T_{RbF} \approx 590$ °C). CIGS type *A* (thinner CDL than that of type *B*) devices degrade with even a small amount of RbF PDT ($T_{RbF} \approx 570$ °C), which can improve the photovoltaic performance of type *B* devices. On the other hand, the photovoltaic performance of CIGS type *C* and *D* devices, which are grown with a thicker CDL than that of type *B*, improve, regardless of $T_{RbF} \approx 570$ or 590 °C. It is found that variations in the photovoltaic efficiencies strongly reflect variations in V_{OC} and FF. These results are consistent with the report by Lepetit *et al.* [40], indicating that the presence of Cu-deficient phases is key to obtaining the beneficial effects of heavy-alkali-halide PDTs.

Figures 8(a) and 8(b) indicate that the elemental Rb concentration in CIGS/CDL films depends on the CDL thickness. A higher Rb concentration is observed in thicker CDL films when the same T_{RbF} is used. It is also found that Rb is likely to concentrate at the surface CDL region, corresponding to the results reported by Kodalle *et al.* [64]. They suggested that Na-Rb exchange was present only in CIGS films with high CGI (>0.8) values [63]. In this study, however, ion-exchange effects of heavy-alkali-metal Rb to Na are observed, even in low CGI films, as represented by the results of the CIGS type *D* films shown in Fig. 8(c). This result suggests that light- and heavy-alkali-metal-ion exchange can occur, irrespective of CGI values, although the effect may depend on GGI because higher GGI values lead to smaller CIGS lattice constants [65], and thus, the incorporation of heavy (large) alkali metals may be diminished.

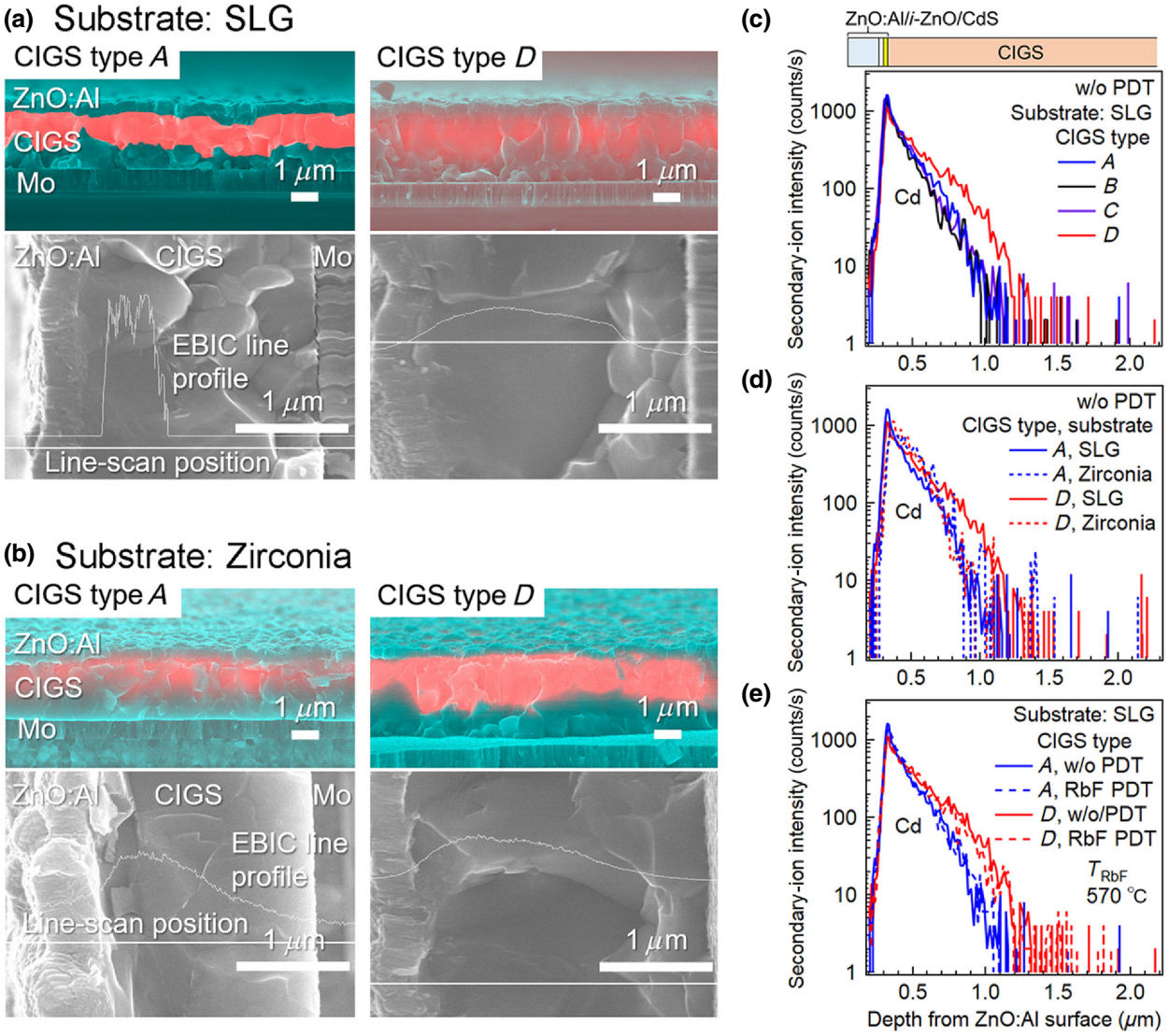

FIG. 6. SEM and EBIC images and corresponding EBIC line profiles obtained from CIGS type *A* and *D* solar-cell devices grown on SLG (a) and zirconia (b) substrates. EBIC measurements are performed using an acceleration voltage of 15 kV. (c) Elemental Cd SIMS depth profiles in CIGS type *A*, *B*, *C*, and *D* devices grown w/o RbF PDT. (d) SIMS elemental distribution profiles of Cd in CIGS type *A* and *D* devices grown on SLG and zirconia substrates without RbF PDT. (e) SIMS Cd distribution profiles in CIGS type *A* and *D* devices grown on SLG substrates with and without RbF PDT.

One of the distinctive effects of heavy-alkali-halide PDTs is the formation of Cu-depletion surfaces [32,66,67]. It is observed that RbF PDT performed on CIGS type *A* (CGI $>$ 0.8 at the surface) enhances Cu deficiency, whereas CIGS type *D* (CGI $<$ 0.6 at the surface) shows enhanced Ga diffusion to the surface CDL, rather than Cu depletion, as shown in Fig. 8(d). Also, Ga diffusion increases with increasing T_{RbF}, that is, with increasing RbF supply, as shown in Fig. 8(e). This result is supportive of a surface-modification model suggested in the literature [40], in which F (originating from RbF) is likely to react with Ga to form GaF_3, which is removed during the CBD process for CdS deposition, resulting in an In-rich (low GGI) surface for the case of conventional double-graded GGI profile CIGS films. Namely, it is suggested that elemental F attracts Ga and enhances Ga diffusion from the CIGS to the surface CDL region. The GGI values at the surface of CIGS type *A*-*D* films used in this study are very low ($<$ 0.03), as can be seen in Table I. In such low-GGI-surface films, therefore, the affinity of F and Ga might be more readily apparent as enhanced Ga diffusion to the surface CDL region with increasing RbF PDT.

Variations in the PL spectra observed from CIGS type *A*-*D* films grown on SLG and zirconia substrates are shown in Figs. 9(a) and 9(c), respectively. The PL peak intensity decreases with increasing CDL thickness, varying from

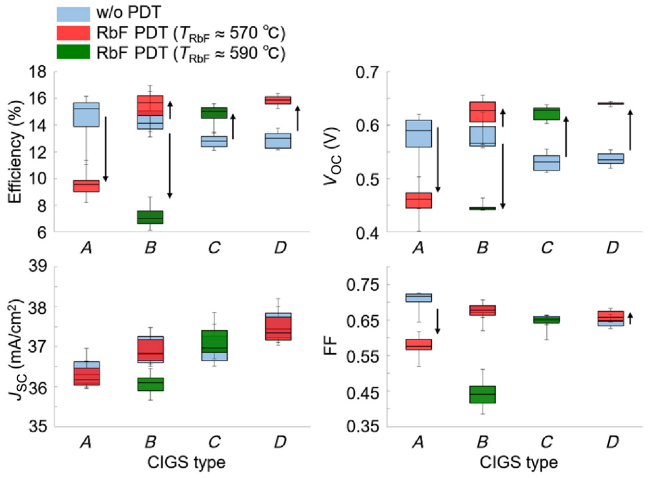

FIG. 7. Solar-cell parameter variations obtained with RbF PDT performed on CIGS type *A*, *B*, *C*, and *D* devices grown on SLG substrates. Arrows indicate variation trends observed with each RbF PDT condition.

CIGS type *A* to *D*, irrespective of substrate materials, except for the low PL peak intensity of the CIGS type *A* film grown on a SLG substrate. A clear correlation between the PL peak intensity variation and the photovoltaic performance shown in Figs. 2(a) and 2(b) is observed. The low peak intensity of the CIGS type *A* film grown on SLG is attributable to the high CGI value (>1), as shown in Table I, indicating the possibility that the presence of segregated Cu_xSe phases [68] in the film leads to a deterioration in CIGS film properties [69]. Although CIGS type *A* devices grown on SLG substrates demonstrate relatively high photovoltaic performance, as shown in Fig. 2(a), the wide error range (broad dispersion of values) observed in, for example, the efficiency values from 11% to 16% may be due to residual Cu_xSe phases in CIGS type *A* films. It is found that variations in the PL peak intensity observed with RbF PDT correspond to the trends observed in the photovoltaic performance shown in Fig. 7, that is, an increase in the PL intensity corresponds to improvements in device performance (efficiency, V_{OC}, and FF) and vice versa. In contrast to this reasonable correlation between the PL peak intensity and photovoltaic performance variations, variations observed in the PL lifetimes shown in Figs. 9(b) and 9(d) do not follow the variational trend in the photovoltaic performance.

Figures 9(b) and 9(d) show TRPL transients measured using the corresponding CIGS samples shown in Figs. 9(a) and 9(c), respectively. The PL decay is analyzed using the following biexponential function:

$$I_{PL}(t) = C_1 exp(-t/\tau_1) + C_1 exp(-t/\tau_1), \qquad (2)$$

where $I_{PL}(t)$ represents the PL intensity, C_1 and C_2 are coefficients, and τ_1 and τ_2 are decay times. The τ_1 and τ_2

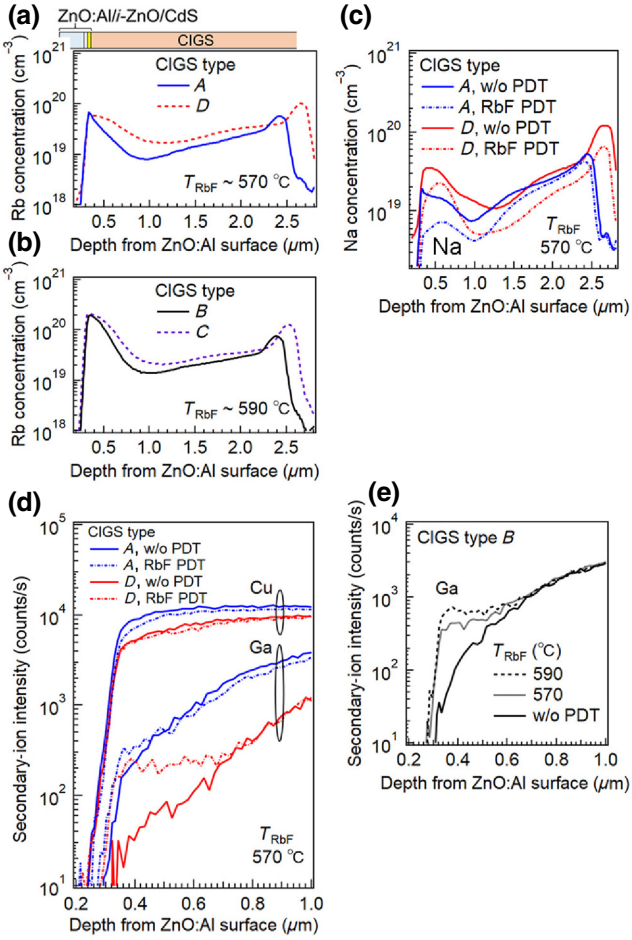

FIG. 8. SIMS elemental distribution profiles of Rb in CIGS type *A* and *D* films grown with RbF PDT using a T_{RbF} of 570 °C (a), and in CIGS type *B* and *C* films grown with RbF PDT using a T_{RbF} of 590 °C (b). (c) SIMS elemental distribution variations of Na in CIGS type *A* and *D* films with RbF PDT. (d) Elemental Cu and Ga SIMS distribution variations obtained from CIGS type *A* and *D* films with RbF PDT. (e) Elemental Ga SIMS distribution variations obtained from CIGS type *B* films with RbF PDT.

values obtained are summarized in Table II. Although the PL peak intensity decreases with increasing CDL thickness from CIGS type *A* to *D*, the lifetime improves with increasing CDL thickness. It should be noted here that the photovoltaic performance degrades with increasing CDL thickness, as shown in Figs. 2(a) and 2(b). On the other hand, improvements in the lifetime observed with RbF PDT correspond to an increase in the PL peak intensity and concomitant improvements in photovoltaic performance. Thus, there are at least two different mechanisms behind the improvements in the lifetime. The nominal lifetime improvements observed with increasing CDL thickness are possibly due to defect-level (E_D) formation [III_{Cu} (III, group III element, In or Ga)]. III_{Cu} defects are reported to form relatively deep energy levels [28] (a model in which the In_{Cu} antisite defect in $CuInSe_2$ can be a shallow donor,

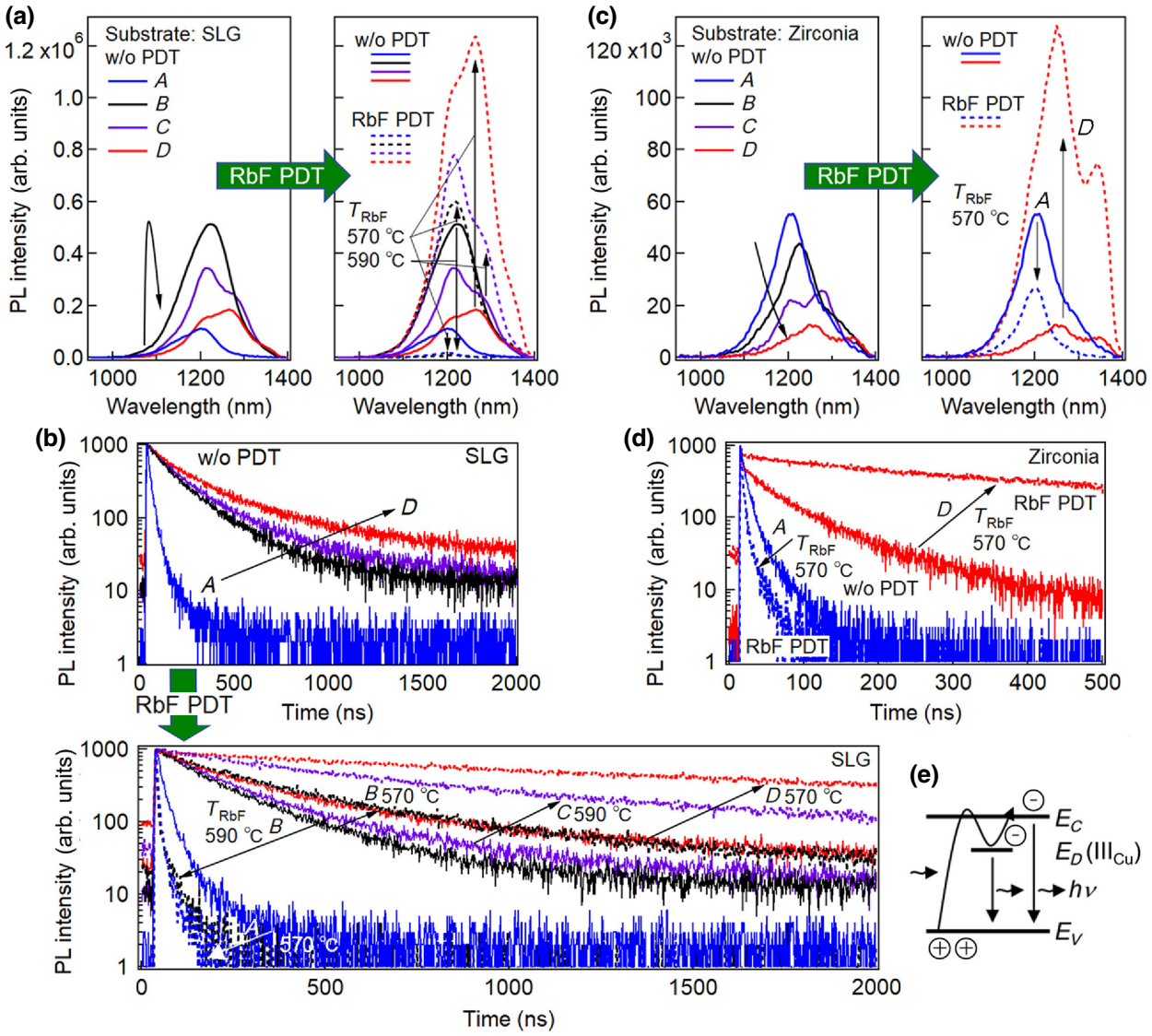

FIG. 9. PL spectra obtained from CIGS type *A*, *B*, *C*, and *D* films grown on SLG (a) and zirconia (c) substrates with and without RbF PDT. (b),(d) TRPL transients measured using the same CIGS samples. Sample structure used is substrate/Mo/CIGS/CDL/CdS (without ZnO layers). Measurements are carried out at room temperature with an excitation light source of 532 nm, 0.31 mW (PL), and 0.11 mW (TRPL), and a spot size of about 1 mm^2. (e) Schematic energy diagram corresponding to PL in thick CDL samples, such as CIGS type *D*. E_C, E_V, h, and ν are the conduction-band minimum, valence-band maximum, Planck constant, and frequency, respectively.

whereas Ga_{Cu} in $CuGaSe_2$ can be deep is also reported [70]), and thus, are expected to act as nonradiative recombination centers and/or cause PL in the long-wavelength region, as can be seen in the PL spectra of the CIGS type *D* films shown in Fig. 9(c). Due to the enhancement of the formation of the defect-level E_D with increasing t_{3rd} from CIGS types *A* to *D*, an increase in the probability of the E_D-E_C transition shown in Fig. 9(e) is expected, even at room temperature. This can increase the nominal lifetime, as observed by the TRPL measurements, but, in fact, may be associated with a longer trapping time, and this phenomenon does not indicate improvements in film quality, as manifested by the degradation in the PL intensity and photovoltaic performance. Also, it should be noted here that the CGI ratio and GGI affect the PL peak position. The dependence of the PL peak position on the CGI can be explained by changes in the potential fluctuation amplitudes. Namely, when fluctuations increase, the carriers occupy deeper states in the band gap and the luminescence signal redshifts [71]. This effect also should be considered in the interpretation of the PL peak shifts observed in Figs. 9(a) and 9(c) and the TRPL results in Figs. 9(b) and 9(d). On the other hand, improvements in the lifetime with concomitant increases in the PL peak intensity and

TABLE II. Variations in τ_1 and τ_2 values calculated from curve fitting performed on TRPL results shown in Fig. 9(b).

CIGS type	RbF PDT	Wavelength (nm)	τ_1 (ns)	τ_2 (ns)
A	No	1205	18	69
B	No	1225	133	409
C	No	1220	137	483
D	No	1255	179	784
A	Yes	1205	5	25
B	Yes	1225	201	656
C	Yes	1225	281	951
D	Yes	1260	347	1770

enhancements in photovoltaic performance observed with RbF PDT are substantial improvements, which lead to a reduction of recombination at the interface and in the bulk (including the grain boundaries in the film).

The deterioration of the lifetime observed from CIGS type *A* devices with RbF PDT shown in Figs. 9(b) and 9(d) is attributable to the formation of defects, which act as recombination centers at the CIGS/CdS interface with RbF PDT. When the CDL is not thick enough, it is found that even a small amount RbF PDT ($T_{\mathrm{RbF}} \approx 570\,^{\circ}\mathrm{C}$) leads to deterioration in the PL intensity, as shown in Figs. 9(a), and in the photovoltaic performance, as shown in Figs. 7. External quantum efficiency (EQE) curves measured with the use of various bias voltages for CIGS type *A* and *D* devices are shown in Figs. 10(a)–10(d). When a pronounced recombination in the bulk of the film is present, a decreasing EQE with increasing forward-bias voltage in the long-wavelength region is expected because a decreasing electric field with an increasing bias voltage limits carrier collection due to increasing recombination in the bulk. On the other hand, when recombination at the CIGS/CdS interface region is dominant, the EQE loss is independent of the wavelength or, if the recombination rate near the interface region is extremely high, the loss will appear in the short-wavelength region. As shown in Fig. 10(b), the ΔEQE loss in the wavelength region of 400–500 nm is observed only for a CIGS type *A* device grown with RbF PDT (indicated by the arrow), indicating the small value of the collection function of the CIGS film surface region close to the interface. A similar result is obtained on alkali-free zirconia substrates as well (not shown).

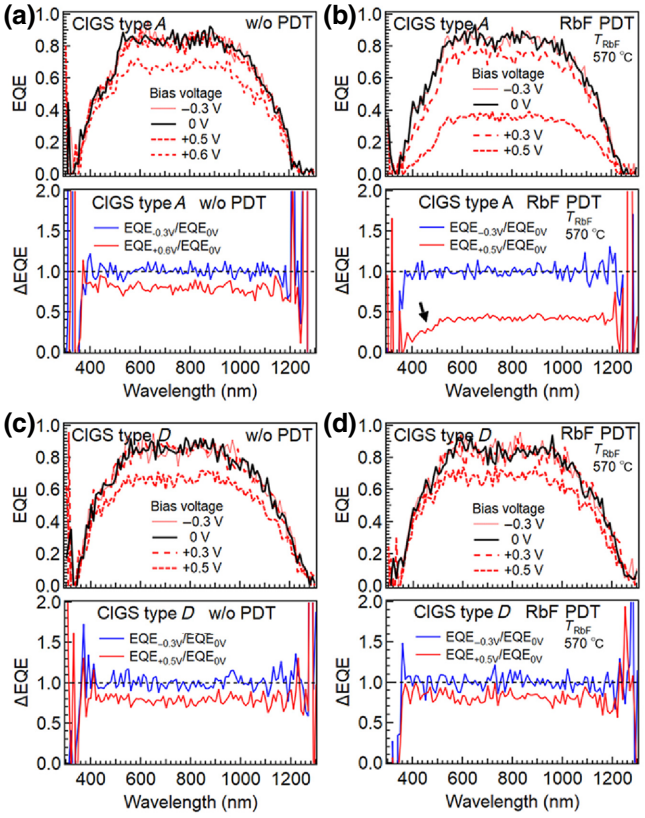

FIG. 10. EQE variations measured with bias voltages for CIGS type *A* devices grown on SLG substrates without (a) and with (b) RbF PDT, and likewise for CIGS type *D* devices (c),(d).

C. Metastable acceptor formation with light-soaking treatments

Metastable phenomena, which are often observed in CIGS solar cells and known as light-soaking or bias-soaking effects, resulting in enhancements in photovoltaic performance (V_{OC}, FF, and efficiency) [72–80], are investigated as a function of CDL thickness and RbF PDT using CIGS type *A*-*D* devices. At present, a model based upon intrinsic metastable defect formation in CIGS, such as a Se-Cu complex vacancy, V_{Se}-V_{Cu}, which is activated by illumination or bias voltage, resulting in the capture of free electrons ($[V_{\mathrm{Se}}\text{-}V_{\mathrm{Cu}}]^{+} + 2e^{-} \rightarrow [V_{\mathrm{Se}}\text{-}V_{\mathrm{Cu}}]^{-}$) and hole emission ($[V_{\mathrm{Se}}\text{-}V_{\mathrm{Cu}}]^{+} \rightarrow [V_{\mathrm{Se}}\text{-}V_{\mathrm{Cu}}]^{-} + 2h^{+}$), where e^{-} and h^{+} are electron and hole, respectively, is probable and can explain the gist of metastable acceptor formation in CIGS [75]. Nonetheless, the correlation between metastable acceptor formation and alkali-metal doping effects is still open to discussion.

N_{CV} variations with LS treatments obtained from CIGS type *A*-*D* devices grown without RbF PDT are shown in Figs. 11(a) and 11(b). A substantial increase in N_{CV} is obtained with LS treatments, regardless of the CDL thickness and substrate material. The ratios of increasing N_{CV} with LS treatments ($N_{\mathrm{CVLS}}/N_{\mathrm{CVinitial}}$) for these devices are shown in Table III. Interestingly, the $N_{\mathrm{CVLS}}/N_{\mathrm{CVinitial}}$ values obtained from CIGS devices grown on SLG and zirconia substrates are approximately 3 and 10, respectively, and these values remain nearly constant for all devices, irrespective of the CDL thickness. This result indicates that CIGS films grown on SLG substrates have higher N_{CV} values than those of films grown on zirconia substrates before LS treatment, most likely due to the presence of

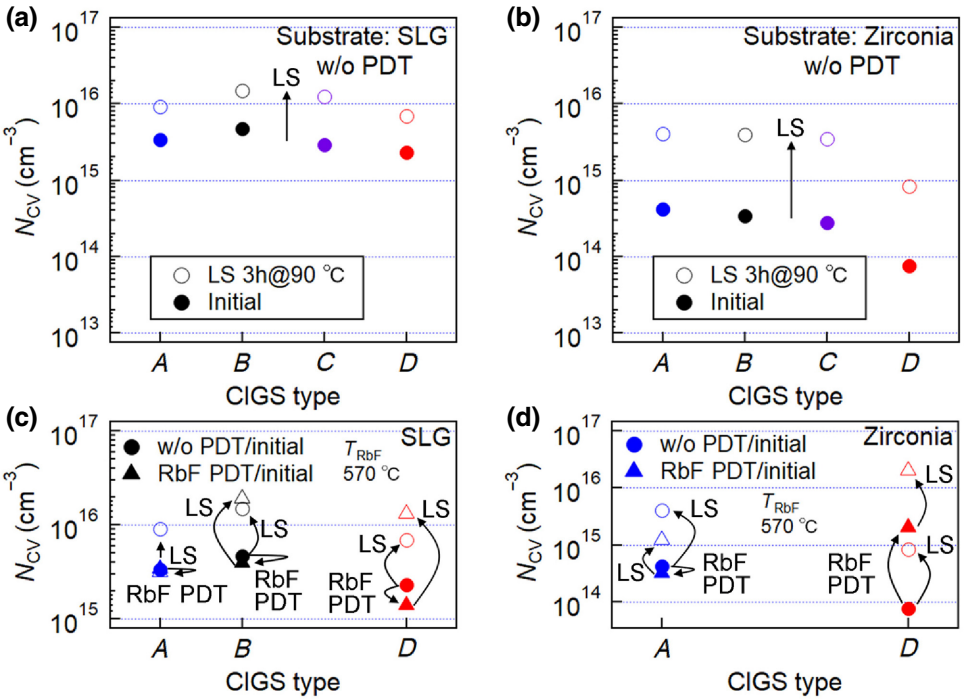

FIG. 11. Variations in N_{CV} values with LS treatments calculated from *C-V* measurements at 0 V obtained from CIGS type *A*, *B*, *C*, and *D* devices grown on alkali-containing SLG (a) and alkali-free zirconia (b) substrates. (c),(d) Comparisons of variations in N_{CV} values with LS treatments obtained from CIGS devices without and with RbF PDT. Solid circles indicate initial N_{CV} values (N_{CV} before LS) obtained for w/o PDT devices. Open circles indicate N_{CV} values obtained after LS. Solid and open triangles indicate N_{CV} values obtained before and after LS, respectively, for RbF PDT devices.

Na_{Cu} substitutional defects, which reduce the number of donor-type III_{Cu} defects. The formation of Na_{Cu} is also expected to reduce the number of V_{Cu} (V_{Se}-V_{Cu}) defects, resulting in smaller $N_{CVLS}/N_{CVinitial}$ values than those of alkali-free CIGS devices grown on zirconia substrates. On the other hand, the N_{CV} values observed from CIGS films grown on zirconia substrates before LS treatment are small ($\sim 10^{14}$ cm^{-3}), probably due to the presence of a large quantity of III_{Cu} and V_{Cu} (V_{Se}-V_{Cu}) defects. Therefore, the $N_{CVLS}/N_{CVinitial}$ values of these CIGS films are large, but the final N_{CV} values observed after LS treatments are still smaller than those of alkali-containing CIGS films due to compensation deriving from the presence of a large number of residual donor-type defects in the alkali-free CIGS films.

The correlation between the effects of RbF PDT and LS treatments are shown with a focus upon CIGS types *A* and *D*, that is, thin and thick CDL devices in Figs. 11(c) and 11(d). A decrease in N_{CV} values with RbF PDT is observed in CIGS devices grown on SLG substrates, regardless of the CDL thickness. This result is attributable to the elimination of Na from the CIGS films due to the heavy-alkali-halide RbF PDT, similar to the case of KF PDT reported in the literature [32]. As shown in Fig. 11(c), the CIGS type *B* and *D* devices grown on SLG substrates with RbF PDT show an increase in N_{CV} with LS treatment and the final N_{CV} values are larger than those of CIGS devices grown without RbF PDT. This result suggests that RbF PDT and LS treatments enhance metastable acceptor formation through the modification of Na-related defects, such as Na_{Cu} to V_{Cu} (V_{Se}-V_{Cu}), and/or newly formed Rb-related defects, which enhance the metastability. On the other hand, an alkali-free CIGS type *D* device shows an increase in N_{CV} with RbF PDT in Fig. 11(d), implying that Rb has the effect of increasing N_{CV}, although the effect of Na is likely greater [37]. The performance of CIGS type *A* devices shown in Figs. 11(c) and 11(d) degrades with RbF PDT, irrespective of the substrate material. This result suggests that the amount of RbF PDT performed at $T_{RbF} \approx 570$ °C is excessive for such thin CDL devices and leads to the formation of harmful defects, rather than beneficial effects.

TABLE III. Variations in the ratio of increasing N_{CV} values after LS treatments ($N_{CVLS}/N_{CVinitial}$) obtained from CIGS type *A*, *B*, *C*, and *D* devices grown on SLG and zirconia substrates.

CIGS type	Substrate	$N_{CVLS}/N_{CVinitial}$
A	SLG	2.7
B	SLG	3.2
C	SLG	4.3
D	SLG	3.0
A	Zirconia	9.7
B	Zirconia	11.4
C	Zirconia	12.5
D	Zirconia	10.8

Typical variations in solar-cell parameters with LS treatment obtained from CIGS type *A*-*D* devices grown on SLG and zirconia substrates without RbF PDT are shown in Figs. 12(a) and 12(b), respectively. Current density (J)-V curves obtained from corresponding CIGS type *A* and *D* devices are shown in Figs. 13(a) and 13(b). Improvements in photovoltaic efficiency with LS treatment are observed

from thick CDL (CIGS type *C* and *D*) devices, though the initial photovoltaic efficiencies of thick CDL devices are relatively low, and thus, the efficiencies of the thin CDL devices (type *A* and *B*) are still superior, even after LS treatment. These single-graded GGI devices grown with thick CDL conditions show significant improvements in FF values, rather than V_{OC}, and a decrease in J_{SC} values with LS treatment. The *J-V* curve variations observed with LS treatment are very informative for interpreting these solar-cell parameter variations. The *J-V* curves obtained from CIGS type *A* and *D* devices grown on SLG substrates without PDT show no significant distortion in the fourth quadrant, as shown in Fig. 13(a), whereas the CIGS type *D* device grown on a zirconia substrate shows a significant distortion [Fig. 13(b)]. There are various models suggested for the observation of such *J-V* curve distortions [81–85]. The so-called red-kink behavior is a typical example and well known as being a CdS buffer and concomitant CIGS/CdS interface-based phenomenon, namely, a low free-electron density in the CdS buffer layer (acceptor-type mid-gap defect) causes an increase in E_C, resulting in an electron barrier at the CIGS/CdS interface with increasing forward-bias voltage and a thicker CdS layer enhances barrier effects [81–83]. The alkali-free CIGS type *D* film is expected to have a very low hole-carrier density, as shown in Fig. 11(b), and this leads to a drop of E_C and an increase in resistivity. As a consequence, the same effect, leading to an increase in the E_C of the CdS layer, is expected to occur, resulting in an increase in the electron barrier at the CDL/CdS interface shown in Fig. 13(e) with increasing forward-bias voltage. It should be noted that the CDL, which consists of OVCs, may have a lower E_C value than that of a I-III-VI_2 phase of CIGS [16,28,30,86], and thus, the CDL/CdS interface barrier effect is expected to be more pronounced in alkali-free CIGS devices, even under white illumination, as shown in Fig. 13(b).

RbF PDT is found to enhance the *J-V* curve distortion. Variations in *J-V* curves obtained with LS treatment from CIGS type *A* and *D* devices grown with RbF PDT are shown in Figs. 13(c) and 13(d). These devices show a pronounced distortion in the fourth quadrant. There are two models, which are based on the CIGS-surface (the CIGS/CdS interface) and back-surface (the Mo/CIGS interface) issues, suggest the distortion observed with RbF PDT. One is the formation of a high and thick electron barrier at the CIGS (CDL)/CdS interface due to Rb-In-Se phases. $RbInSe_2$ is suggested to have a relatively wide E_g value of 2.0–2.6 eV [87,88]. Not only Rb, but alkali-In-Se_2 phases such as $NaInSe_2$, $KInSe_2$ and $CsInSe_2$, tend to have wider E_g values than $CuInSe_2$ [88]. Taking the effects of Cu-Rb exchange into account, the widening of E_g is likely to occur due to an E_V drop, rather than the modification of E_C [38], because the valence band of CIGS consists of Cu 3*d* orbitals [28]. However, if the Fermi level (E_F) is located in the middle of the band gap, an increase in

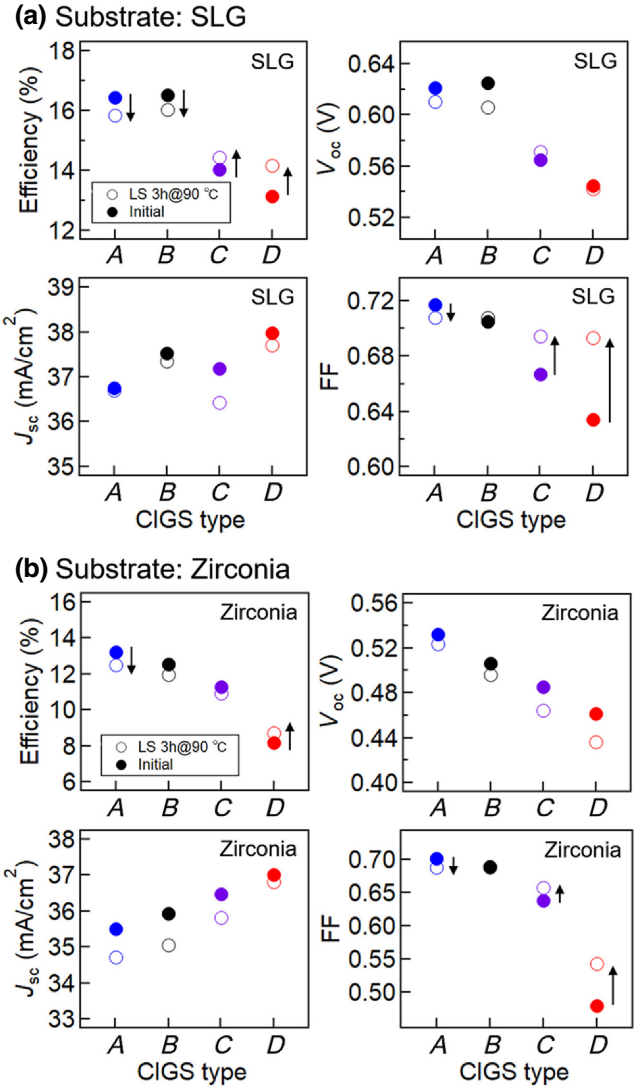

FIG. 12. Variations in solar-cell parameters with LS treatment obtained from CIGS type *A*, *B*, *C*, and *D* devices grown on SLG (a) and zirconia (b) substrates (without RbF PDT).

E_C is also possible. This can form an electron barrier at the CDL/CdS interface [39,84] and is expected to lead to the *J-V* curve distortion shown in Figs. 13(c) and 13(d). Here, the CDL is assumed to be *n* type [16,89], and thus, the value of E_F is close to E_C rather than E_V. The other model suggested is that heavy-alkali metals replace Na at the Mo/CIGS interface, which can lead to the formation of a barrier [37,62,90,91]. Certainly, a decrease in the Na concentration at the Mo/CIGS interface is observed with RbF PDT, as shown in Fig. 8(c). It can be, however, observed in Fig. 13(b) that the Na-free CIGS type *A* device shows no significant distortion, and thus, this model may not be relevant for the CIGS devices used in this study. The CIGS (CDL)/CdS interface issues are, therefore, considered to be the dominant reason for the *J-V* curve distortions observed. The variation in *J-V* curve shapes shown in

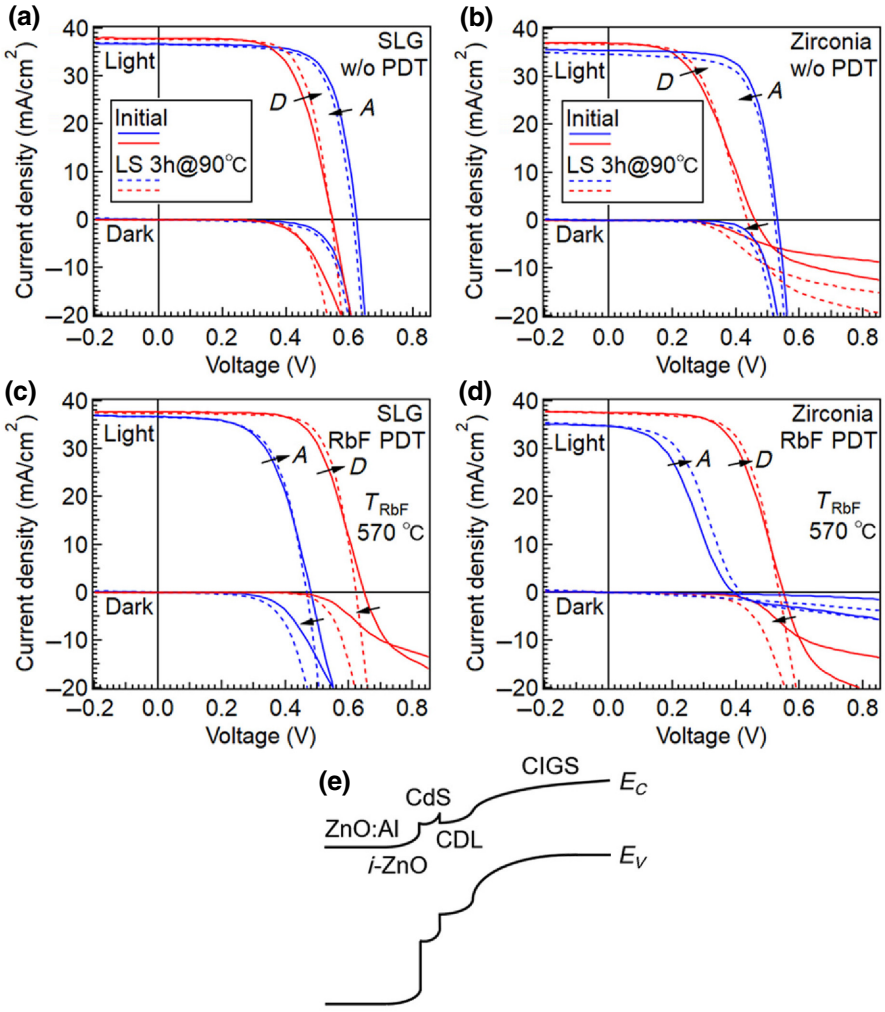

FIG. 13. Variations in *J-V* curves observed with LS treatment from CIGS type *A* and *D* devices grown without PDT on SLG (a) and zirconia (b) substrates and with RbF PDT on SLG (c) and zirconia (d) substrates. (e) Schematic of the energy-band diagram for CIGS type *D* devices grown without PDT.

Figs. 13(a)–13(d) implies that CIGS device performance improves with LS treatment, except for the type *A* devices grown without PDT. The variations observed with LS treatment (improvements in FF and a decrease in V_{OC} with the mitigation of *J-V* curve distortion) are attributable to an increase in N_{CV} and a concomitant decrease in the series resistance, resulting in an increase in the E_C of CIGS, in comparison with that of CdS, and/or Rb compound phases, and thus, a reduction of the barrier effect present at the CDL/CdS interface.

Enhancements in single-graded E_C device performance with LS treatment have been reported with $Cu(In, Ga(S, Se)_2$ in the literature [92]. In this case, the presence of elemental S is expected to play a role in reducing E_V, resulting in the formation of a hole barrier at the interface, which is similar to the role of CDL in this study, and a decrease in recombination. Thus, the performance deterioration observed with LS treatment for the CIGS type *A* devices can be attributed to the lack of such a functional interface to suppress recombination.

Variations in the EQE curves with LS treatment observed from CIGS type *A-D* devices are shown in Figs. 14(a)–14(e). When a large number of defects are present in the bulk of a CIGS film, a decrease in the EQE in the long-wavelength region with increasing N_{CV} from LS treatment is expected. This trend can be observed in CIGS devices grown on alkali-free zirconia substrates, as shown in Fig. 14(b), although improvements in EQE with RbF PDT can also be found in Fig. 14(d). An important finding of this study is that the relatively thick CDL devices (type *B-D*) show an increase in EQE in the long-wavelength region over the range of 1200–1350 nm with LS treatment. This variation is found to be reversible and reversion to the initial EQE values is observed after storage of the devices in the dark for several days. Also, this EQE variation is observed independently of the substrate material and RbF PDT. At present, it is suggested that defects formed in the CDL are activated with LS treatment and lead to energy-band fluctuations and/or tailing [93] and enable the film to absorb long-wavelength light, although there is room for

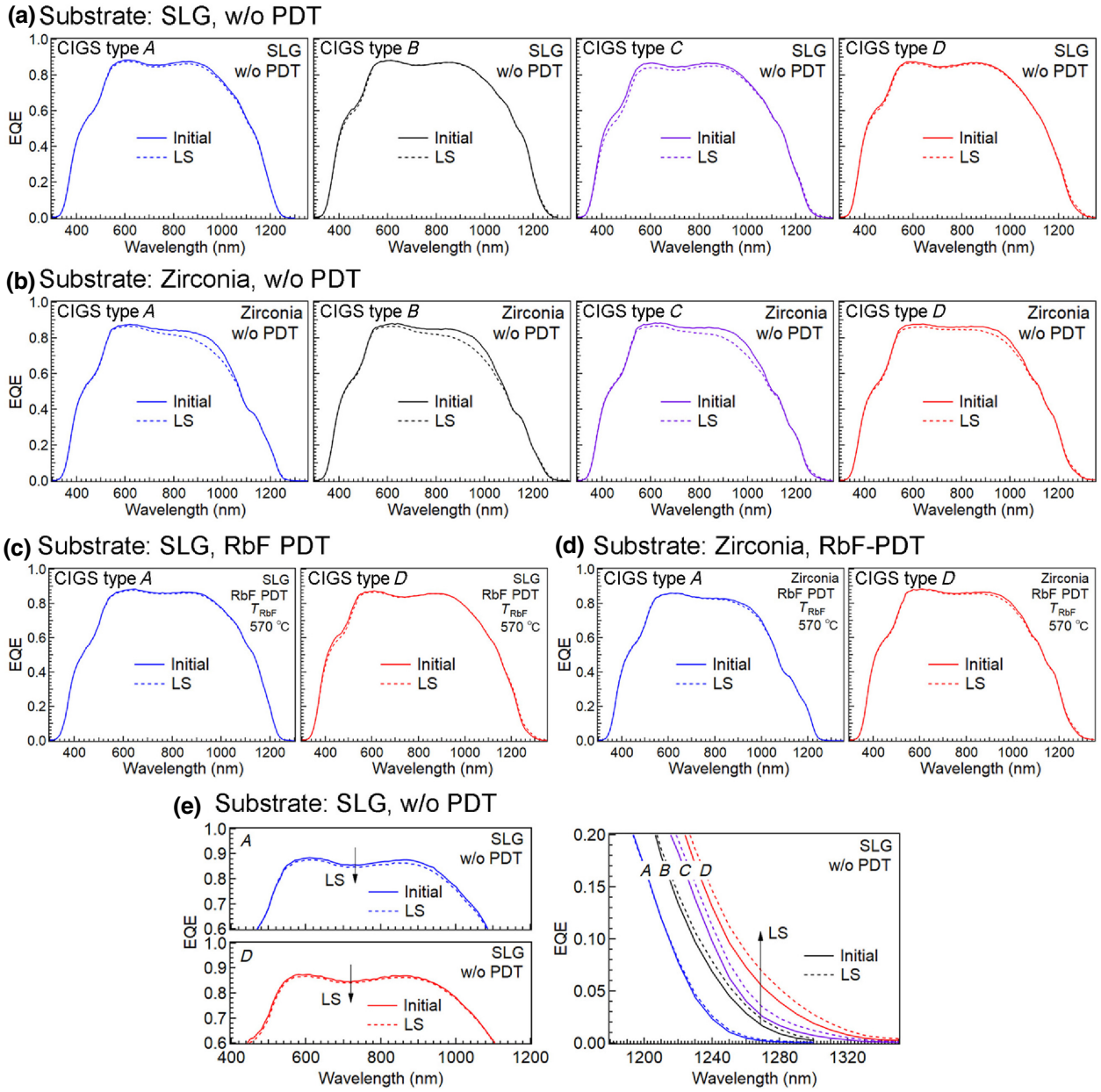

FIG. 14. Variations in EQE curves with LS treatment (for 3 h at 90 °C) obtained from CIGS type *A*, *B*, *C*, and *D* devices grown on SLG (a) and zirconia (b) substrates without RbF PDT, and with RbF PDT (c),(d). Pronounced variations observed in these EQE curves are magnified in (e).

further investigation into the detailed mechanism behind this EQE increase.

IV. CONCLUSIONS

The effects of the CDL present in CIGS solar-cell devices are investigated, with a focus upon the thickness and the effects of alkali-metal doping. The CDL thickness is found to vary the results of RbF PDT and the use of a thick CDL leads to an enhancement in the beneficial effects of RbF PDT over a relatively wide range of RbF supply, whereas the use of a thin CDL is likely to lead to a deterioration in device performance, with even a small amount of RbF PDT. This result is attributable to defect formation, which results in increased recombination in the CIGS-film-surface region. Elemental Ga diffusion to the surface CDL from the CIGS bulk with RbF PDT is observed, and this result is supportive of a model of Ga-F compound formation with alkali-fluoride PDT [40], although further investigation using various alkali-compound sources is required to reach a definitive conclusion. The observation of a decrease in the PL peak intensity with increasing

CDL thickness is attributable to an increase in nonradiative carrier recombination centers originating from deep defect states, such as III_{Cu}. Metastable acceptor formation is observed independently of the CDL thickness, implying that the dominant mechanism behind the metastability originates from CIGS bulk issues, rather than interface factors.

The effective utilization of Cu-deficient phases as a functional material is expected to be key to open a frontier of a wide variety of energy-conversion devices, such as not only photovoltaic solar cells, but also photocathodes for water-splitting hydrogen generation. This study underscores the role and effects of a CDL present in CIGS solar-cell devices grown with alkali-metal doping. The CDL is found to play an important role in CIGS devices and lead to changes in alkali-metal doping effects, as well as changes in the energy-band structure near the *p*-*n* interface region.

ACKNOWLEDGMENTS

The authors thank H. Higuchi, H. Takahashi, and M. Iioka for their help with the experiments and technical support. The authors also thank H. Shibata, J. Nishinaga, and Y. Kamikawa for their valuable insights. This work is supported by a Mitsubishi Foundation Research Grant in the Natural Sciences No. 201910001; JSPS KAKENHI Grant No. 19K05282; and partly by the New Energy and Industrial Technology Development Organization (NEDO) under the Ministry of Economy, Trade and Industry (METI).

[1] M. Powalla, S. Paetel, E. Ahlswede, R. Wuerz, C. D. Wessendorf, and T. Magorian Friedlmeier, Thin-film solar cells exceeding 22% solar cell efficiency: An overview on CdTe-, Cu(In, Ga)Se_2-, and perovskite-based materials, Appl. Phys. Rev. **5**, 041602 (2018).

[2] S. Niki, M. Contreras, I. Repins, M. Powalla, K. Kushiya, S. Ishizuka, and K. Matsubara, CIGS absorbers and processes, Prog. Photovolt. **18**, 453 (2010).

[3] K. Sakurai, H. Tomita, D. Schmitz, S. Tokuda, K. Ogawa, H. Shibata, and A. Masuda, Exploring suitable damp heat and potential induced degradation test procedures for Cu(In, Ga)(S, Se) photovoltaic modules, Jpn. J. Appl. Phys. **57**, 08RG02 (2018).

[4] X. Hu, P. Jood, M. Ohta, M. Kunii, K. Nagase, H. Nishiate, M. G. Kanatzidis, and A. Yamamoto, Power generation from nanostructured PbTe-based thermoelectrics: Comprehensive development from materials to modules, Energy Environ. Sci. **9**, 517 (2016).

[5] T. Wang, K. Zhao, P. Qui, Q. Song, L. Chen, and X. Shi, Aguilarite Ag_4SSe thermoelectric material: Natural mineral with low lattice thermal conductivity, ACS Appl. Mater. Interfaces **11**, 12632 (2019).

[6] W.-X. Zhou, D. Wu, G. Xie, K.-Q. Chen, and G. Zhang, Ag_2S: A ductile thermoelectric material with high ZT, ACS Omega **5**, 5796 (2020).

[7] S. N. Guin, A. Chatterjee, D. S. Negi, R. Datta, and K. Biswas, High thermoelectric performance in tellurium free p-type $AgSbSe_2$, Energy Environ. Sci. **6**, 2603 (2013).

[8] Y. Chen, X. Feng, M. Liu, J. Su, and S. Shen, Towards efficient solar-to-hydrogen conversion: Fundamentals and recent progress in copper-based chalcogenide photocathodes, Nanophotonics **5**, 524 (2016).

[9] B. Marsen, B. Cole, and E. L. Miller, Photoelectrolysis of water using thin copper gallium diselenide electrodes, Sol. Energy Mater. Sol. Cells **92**, 1054 (2008).

[10] L. Zhang, T. Minegishi, M. Nakabayashi, Y. Suzuki, K. Seki, N. Shibata, J. Kubota, and K. Domen, Durable hydrogen evolution from water driven by sunlight using (Ag, Cu)$GaSe_2$ photocathodes modified with CdS and $CuGa_3Se_5$, Chem. Sci. **6**, 894 (2015).

[11] H. Kumagai, T. Minegishi, N. Sato, T. Yamada, J. Kubota, and K. Domen, Efficient solar hydrogen production from neutral electrolytes using surface-modified Cu(In, Ga)Se_2 photocathodes, J. Mater. Chem. A **3**, 8300 (2015).

[12] M. Moriya, T. Minegishi, H. Kumagai, M. Katayama, J. Kubota, and K. Domen, Stable hydrogen evolution from CdS-modified $CuGaSe_2$ photoelectrode under visible-light irradiation, J. Am. Chem. Soc. **135**, 3733 (2013).

[13] T. J. Jacobsson, V. Fjällström, M. Sahlberg, M. Edoff, and T. Edvinsson, A monolithic device for solar water splitting based on series interconnected thin film absorbers reaching over 10% solar-to-hydrogen efficiency, Energy Environ. Sci. **6**, 3676 (2013).

[14] C. P. Muzzillo, W. E. Klein, Z. Li, A. D. DeAngelis, K. Horsley, K. Zhu, and N. Gaillard, Low-Cost, efficient, and durable H_2 production by photoelectrochemical water splitting with $CuGa_3Se_5$ photocathodes, ACS Appl. Mater. Interfaces **10**, 19573 (2018).

[15] D. Lincot, H. G. Meier, J. Kessler, and J. Vedel, Photoelectrochemical study of p-type copper indium diselenide thin films for photovoltaic applications, Sol. Energy Mater. **20**, 67 (1990).

[16] D. Schmid, M. Ruckh, F. Grunwald, and H. W. Schock, Chalcopyrite/defect chalcopyrite heterojunctions on the basis of $CuInSe_2$, J. Appl. Phys. **73**, 2902 (1993).

[17] T. Negami, N. Kohara, M. Nishitani, T. Wada, and T. Hirao, Preparation and characterization of $Cu(In_{1-x}Ga_x)_3Se_5$ thin films, Appl. Phys. Lett. **67**, 825 (1995).

[18] C. Rincón, S. M. Wasim, G. Marín, J. M. Delgado, J. R. Huntzinger, A. Zwick, and J. Galibert, Raman spectra of the ordered vacancy compounds $CuIn_3Se_5$ and $CuGa_3Se_5$, Appl. Phys. Lett. **73**, 441 (1998).

[19] C. M. Ruiz, X. Fontané, A. Fairbrother, V. Izquierdo-Roca, C. Broussillou, S. Bodnar, A. Pérez-Rodríguez, and V. Bermúdez, Impact of electronic defects on the Raman spectra from electrodeposited Cu(In, Ga)Se_2 solar cells: Application for non-destructive defect assessment, Appl. Phys. Lett. **102**, 091106 (2013).

[20] C. Insignares-Cuello, C. Broussillou, V. Bermúdez, E. Saucedo, A. Pérez-Rodríguez, and V. Izquierdo-Roca, Raman scattering analysis of electrodeposited Cu(In, Ga)Se_2 solar cells: Impact of ordered vacancy

compounds on cell efficiency, Appl. Phys. Lett. **105**, 021905 (2014).
[21] T. Nishimura, H. Sugiura, K. Nakada, and A. Yamada, Accurate control and characterization of Cu depletion layer for highly efficient Cu(In, Ga)Se_2 solar cells, Prog. Photovolt. **27**, 171 (2019).
[22] S. Ji, T. Hayakawa, N. Suyama, K. Nakamura, and A. Yamada, Enhancement of Cu(In, Ga)Se_2 solar cells efficiency by controlling the formation of Cu-deficient layer, Jpn. J. Appl. Phys. **59**, 041003 (2020).
[23] T. Nakada, M. Hongo, and E. Hayashi, Band offset of high efficiency CBD-ZnS/CIGS thin film solar cells, Thin Solid Films **431-432**, 242 (2003).
[24] V. Izquierdo-Roca, R. Caballero, X. Fontané, C. A. Kaufmann, J. Álvarez-García, L. Calvo-Barrio, E. Saucedo, A. Pérez-Rodríguez, J. R. Morante, and H. W. Schock, Raman scattering analysis of Cu-poor Cu(In, Ga)Se_2 cells fabricated on polyimide substrates: Effect of Na content on microstructure and phase structure, Thin Solid Films **519**, 7300 (2011).
[25] S. H. Kwon, S. C. Park, B. T. Ahn, K. H. Yoon, and J. Song, Effect of $CuIn_3Se_5$ layer thickness on $CuInSe_2$ thin films and devices, Sol. Energy **64**, 55 (1998).
[26] B. Namnuan, V. Amornkitbamrung, and S. Chatraphorn, Effects of Cu(In, Ga)$_3Se_5$ defect phase layer in Cu(In, Ga)Se_2 thin film solar cells, J. Alloy. Compd. **800**, 305 (2019).
[27] Sigurd Wagner, J. L. Shay, P. Migliorato, and H. M. Kasper, $CuInse_2$/CdS heterojunction photovoltaic detectors, Appl. Phys. Lett. **25**, 434 (1974).
[28] S. B. Zhang, S.-H. Wei, and A. Zunger, Defect physics of the $CuInSe_2$ chalcopyrite semiconductor, Phys. Rev. B **57**, 9642 (1998).
[29] H. Z. Xiao, L.-Chung Yang, and A. Rockett, Structural, optical, and electrical properties of epitaxial chalcopyrite $CuIn_3Se_5$ films, J. Appl. Phys. **76**, 1503 (1994).
[30] K. Ueda, T. Maeda, and T. Wada, Crystallographic and optical properties of $CuGa_3S_5$, $CuGa_3Se_5$ and $CuIn_3(S, Se)_5$ and $CuGa_3(S, Se)_5$ systems, Thin Solid Films **633**, 23 (2017).
[31] S. M. Wasim, C. Rincón, G. Marín, and J. M. Delgado, On the band gap anomaly in I–III–VI_2, I–III_3–VI_5, and I–III_5–VI_8 families of Cu ternaries, Appl. Phys. Lett. **77**, 94 (2000).
[32] A. Chirilá, P. Reinhard, F. Pianezzi, P. Bloesch, A. R. Uhl, C. Fella, L. Kranz, D. Keller, C. Gretener, H. Hagendorfer, D. Jaeger, R. Erni, S. Nishiwaki, S. Buecheler, and A. N. Tiwari, Potassium-induced surface modification of Cu(In, Ga)Se_2 thin films for high-efficiency solar cells, Nat. Mater. **12**, 1107 (2013).
[33] P. Jackson, R. Wuerz, D. Hariskos, E. Lotter, W. Witte, and M. Powalla, Effects of heavy alkali elements in Cu(In, Ga)Se_2 solar cells with efficiencies up to 22.6%, Phys. Stat. Sol. RRL **10**, 583 (2016).
[34] M. Nakamura, K. Yamaguchi, Y. Kimoto, Y. Yasaki, T. Kato, and H. Sugimoto, Cd-free Cu(In, Ga)$(Se, S)_2$ thin-film solar cell with record efficiency of 23.35%, IEEE J. Photovolt. **9**, 1863 (2019).
[35] P. Reinhard, B. Bissig, F. Pianezzi, H. Hagendorfer, G. Sozzi, R. Menozzi, C. Gretener, S. Nishiwaki, S. Buecheler, and A. N. Tiwari, Alkali-templated surface nanopatterning of chalcogenide thin films: A novel approach toward solar cells with enhanced efficiency, Nano Lett. **15**, 3334 (2015).
[36] L. M. Mansfield, R. Noufi, C. P. Muzzillo, C. DeHart, K. Bowers, B. To, J. W. Pankow, R. C. Reedy, and K. Ramanathan, Enhanced performance in Cu(In, Ga)Se_2 solar cells fabricated by the two-step selenization process with a potassium fluoride postdeposition treatment, IEEE J. Photovolt. **4**, 1650 (2014).
[37] F. Pinanezzi, P. Reinhard, A. Chirilá, B. Bissig, S. Nishiwaki, S. Buecheler, and A. N. Tiwari, Unveiling the effects of post-deposition treatment with different alkaline elements on the electronic properties of CIGS thin film solar cells, Phys. Chem. Chem. Phys. **16**, 8843 (2014).
[38] D. Hauschild, D. Kreikemeyer-Lorenzo, P. Jackson, T. Magorian Friedlmeier, D. Hariskos, F. Reinert, M. Powalla, C. Heske, and L. Weinhardt, Impact of a RbF post-deposition treatment on the electronic structure of the CdS/Cu(In, Ga)Se_2 heterojunction in high-efficiency thin-film solar cells, ACS Energy Lett. **2**, 2383 (2017).
[39] E. Handick, P. Reinhard, J.-H. Alsmeier, L. Köhler, F. Pianezzi, S. Krause, M. Gorgoi, E. Ikenaga, N. Koch, R. G. Wilks, S. Buecheler, A. N. Tiwari, and M. Bär, Potassium postdeposition treatment-induced band gap widening at Cu(In, Ga)Se_2 surfaces – reason for performance leap?, ACS Appl. Mater. Interfaces **7**, 27414 (2015).
[40] T. Lepetit, S. Harel, L. Arzel, G. Ouvrard, and N. Barreau, KF post deposition treatment in co-evaporated Cu(In, Ga)Se_2 thin film solar cells: Beneficial or detrimental effect induced by the absorber characteristics, Prog. Photovolt. **25**, 1068 (2017).
[41] A. M. Gabor, J. R. Tuttle, D. S. Albin, M. A. Contreras, R. Noufi, and A. M. Hermann, High-efficiency $CuIn_xGa_{1-x}Se_2$ solar cells made from $(In_x, Ga_{1-x})_2Se_3$ precursor films, Appl. Phys. Lett. **65**, 198 (1994).
[42] S. Ishizuka, N. Taguchi, J. Nishinaga, Y. Kamikawa, S. Tanaka, and H. Shibata, Group III elemental composition dependence of RbF postdeposition treatment effects on Cu(In, Ga)Se_2 thin films and solar cells, J. Phys. Chem. C **122**, 3809 (2018).
[43] N. Taguchi, S. Tanaka, and S. Ishizuka, Direct insights into $RbInSe_2$ formation at Cu(In, Ga)Se_2 thin film surface with RbF postdeposition treatment, Appl. Phys. Lett **113**, 113903 (2018).
[44] S. Ishizuka, N. Taguchi, and P. J. Fons, Similarities and critical differences in heavy alkali-metal rubidium and cesium effects on chalcopyrite Cu(In, Ga)Se_2 thin-film solar cells, J. Phys. Chem. C **123**, 17757 (2019).
[45] T. Kato, Cu(In, Ga)$(Se, S)_2$ solar cell research in solar frontier: Progress and current status, Jpn. J. Appl. Phys. **56**, 04CA02 (2017).
[46] T. Kato, J.-L. Wu, Y. Hirai, H. Sugimoto, and V. Bermudez, Record efficiency for thin-film polycrystalline solar cells up to 22.9% achieved by Cs-treated Cu(In, Ga)$(Se, S)_2$, IEEE J. Photovolt. **9**, 325 (2019).
[47] R. Scheer and H.-W. Schock, *Chalcogenide Photovoltaics, Physics, Technologies, and Thin Film Devices* (Wiley-VCH Verlag, Weinheim, Germany, 2011), pp. 34.
[48] S. Ishizuka, A. Yamada, P. J. Fons, Y. Kamikawa-Shimizu, H. Komaki, H. Shibata, and S. Niki, Buried p-n junction

formation in $CuGaSe_2$ thin-film solar cells, Appl. Phys. Lett. **104**, 031606 (2014).

[49] K. Sakurai, R. Hunger, R. Scheer, C. A. Kaufmann, A. Yamada, T. Baba, Y. Kimura, K. Matsubara, P. Fons, H. Nakanishi, and S. Niki, In situ diagnostic methods for thin-film fabrication: Utilization of heat radiation and light scattering, Prog. Photovolt. **12**, 219 (2004).

[50] S. Ishizuka, J. Nishinaga, T. Koida, and H. Shibata, An over 18%-efficient completely buffer-free $Cu(In, Ga)Se_2$ solar cell, Appl. Phys. Express **11**, 075502 (2018).

[51] S. Ishizuka, A. Yamada, P. J. Fons, H. Shibata, and S. Niki, Structural tuning of wide-gap chalcopyrite $CuGaSe_2$ thin films and highly efficient solar cells: Differences from narrow-gap $Cu(In, Ga)Se_2$, Prog. Photovolt. **22**, 821 (2014).

[52] D. Rudmann, A. F. da Cunha, M. Kaelin, F. Kurdesau, H. Zogg, A. N. Tiwari, and G. Bilger, Efficiency enhancement of $Cu(In, Ga)Se_2$ solar cells due to post-deposition Na incorporation, Appl. Phys. Lett. **84**, 1129 (2004).

[53] S. Ishizuka, A. Yamada, M. M. Islam, H. Shibata, P. Fons, T. Sakurai, K. Akimoto, and S. Niki, Na-induced variations in the structural, optical, and electrical properties of $Cu(In, Ga)Se_2$ thin films, J. Appl. Phys. **106**, 034908 (2009).

[54] S. Ishizuka, A. Yamada, P. Fons, and S. Niki, Flexible $Cu(In, Ga)Se_2$ solar cells fabricated using alkali-silicate glass thin layers as an alkali source material, J. Renew. Sustain. Energy **1**, 013102 (2009).

[55] M. Marudachalam, H. Hichri, R. Klenk, R. W. Birkmire, W. N. Shafarman, and J. M. Schultz, Preparation of homogeneous $Cu(InGa)Se_2$ films by selenization of metal precursors in H_2Se atmosphere, Appl. Phys. Lett. **67**, 3978 (1995).

[56] S. Ishizuka, L. M. Mansfield, C. DeHart, M. Scott, B. To, M. R. Young, B. Egaas, and R. Noufi, Rapid fabrication of $Cu(In, Ga)Se_2$ thin films by the two-step selenization process, IEEE J. Photovolt. **3**, 476 (2013).

[57] Y. Yan, K. M. Jones, J. Abushama, M. Young, S. Asher, M. M. Al-Jassim, and R. Noufi, Microstructure of surface layers in $Cu(In, Ga)Se_2$ thin films, Appl. Phys. Lett. **81**, 1008 (2002).

[58] M. Maciaszek and P. Zabierowski, The influence of the n-side doping on metastable defect concentrations in $Cu(In, Ga)Se_2$ evaluated from space charge profiles, IEEE J. Photovolt. **5**, 1454 (2015).

[59] T. Nakada and A. Kunioka, Direct evidence of Cd diffusion into $Cu(In, Ga)Se_2$ thin films during chemical-bath deposition process of CdS films, Appl. Phys. Lett. **74**, 2444 (1999).

[60] C.-S. Jiang, F. S. Hasoon, H. R. Moutinho, H. A. Al-Thani, M. J. Romero, and M. M. Al-Jassim, Direct evidence of a buried homojunction in $Cu(In, Ga)Se_2$ solar cells, Appl. Phys. Lett. **82**, 127 (2003).

[61] O. Cojocaru-Mirédin, P. Choi, R. Wuerz, and D. Raabe, Exploring the p-n junction region in $Cu(In, Ga)Se_2$ thin-film solar cells at the nanometer-scale, Appl. Phys. Lett. **101**, 181603 (2012).

[62] J. Keller, O. V. Bilousov, J. Neerken, E. Wallin, N. M. Martin, L. Riekehr, M. Edoff, and C. Platzer-Björkman, Heavy alkali treatment of post-sulfurized $Cu(In, Ga)Se_2$ layers: Effect on absorber properties and solar cell performance, Sol. RRL **4**, 2000248 (2020).

[63] T. Kodalle, T. Bertram, R. Schlatmann, and C. A. Kaufmann, Effectiveness of an RbF post deposition treatment of CIGS solar cells in dependence on the Cu content of the absorber layer, IEEE J. Photovolt. **9**, 1839 (2019).

[64] T. Kodalle, M. D. Heinemann, D. Greiner, H. A. Yetkin, M. Klupsch, C. Li, P. A. van Aken, I. Lauermann, R. Schlatmann, and C. A. Kaufmann, Elucidating the mechanism of an RbF post deposition treatment in CIGS thin film solar cells, Sol. RRL **2**, 1800156 (2018).

[65] S. C. Abrahams and J. L. Bernstein, Piezoelectric nonlinear optic $CuGaS_2$ and $CuInS_2$ crystal structure: Sublattice distortion in $A^IB^{III}C^{VI}_2$ and $A^{II}B^{IV}C^{V}_2$ type chalcopyrites, J. Chem. Phys. **59**, 5415 (1973).

[66] P. Reinhard, B. Bissig, F. Pianezzi, E. Avancini, H. Hagendorfer, D. Keller, P. Fuchs, M. Döbeli, C. Vigo, P. Crivelli, S. Nishiwaki, S. Buecheler, and A. N. Tiwari, Features of KF and NaF postdeposition treatments of $Cu(In, Ga)Se_2$ absorbers for high efficiency thin film solar cells, Chem. Mater. **27**, 5755 (2015).

[67] E. Avancini, R. Carron, T. P. Weiss, C. Andres, M. Bürki, C. Schreiner, R. Figi, Y. E. Romanyuk, S. Buecheler, and A. N. Tiwari, Effects of rubidium fluoride and potassium fluoride postdeposition treatments on $Cu(In, Ga)Se_2$ thin films and solar cell performance, Chem. Mater. **29**, 9695 (2017).

[68] M. L. Fearheiley, The phase relations in the Cu, In, Se system and the growth of $CuInSe_2$ single crystals, Sol. Cells **16**, 91 (1986).

[69] S. Wang, T. Nazuka, H. Hagiya, Y. Takabayashi, S. Ishizuka, H. Shibata, S. Niki, M. M. Islam, K. Akimoto, and T. Sakurai, Depth profile of impurity phase in wide-bandgap $Cu(In_{1-x}, Ga_x)Se_2$ film fabricated by three-stage process, J. Electron. Mater. **47**, 4944 (2018).

[70] S. Siebentritt, Chalcopyrite compound semiconductors for thin film solar cells, Curr. Opin. Green Sustain. Chem. **4**, 1 (2017).

[71] I. Dirnstorfer, Mt. Wagner, D. M. Hofmann, M. D. Lampert, F. Karg, and B. K. Meyer, Characterization of $CuIn(Ga)Se_2$ thin films III. In-rich layers, Phys. Status Solidi A **168**, 163 (1998).

[72] M. N. Ruberto and A. Rothwarf, Time-dependent open-circuit voltage in $CuInSe_2/CdS$ solar cells: Theory and experiment, J. Appl. Phys. **61**, 4662 (1987).

[73] K. Kushiya, M. Tachiyuki, T. Kase, I. Sugiyama, Y. Nagoya, D. Okumura, M. Sato, O. Yamase, and H. Takeshita, Fabrication of graded band-gap $Cu(InGa)Se_2$ thin-film mini-modules with a $Zn(O, S, OH)_x$ buffer layer, Sol. Energy Mater. Sol. Cells **49**, 277 (1997).

[74] M. Igalson, M. Cwil, and M. Edoff, Metastabilities in the electrical characteristics of CIGS devices: Experimental results vs theoretical predictions, Thin Solid Films **515**, 6142 (2007).

[75] S. Lany and A. Zunger, Light- and bias-induced metastabilities in $Cu(In, Ga)Se_2$ based solar cells caused by the $(V_{Se}$-$V_{Cu})$ vacancy complex, J. Appl. Phys. **100**, 113725 (2006).

[76] T. Nakada, T. Kobayashi, T. Kumazawa, and H. Yamaguchi, Impacts of post-treatments on cell performance of

CIGS solar cells with Zn-compound buffer layers, IEEE J. Photovolt. **3**, 461 (2013).

[77] T. Kobayashi, H. Yamaguchi, and T. Nakada, Effects of combined heat and light soaking on device performance of $Cu(In, Ga)Se_2$ solar cells with ZnS(O, OH) buffer layer, Prog. Photovolt. **22**, 115 (2014).

[78] I. Khatri, K. Shudo, J. Matsuura, M. Sugiyama, and T. Nakada, Impact of heat-light soaking on potassium fluoride treated CIGS solar cells with CdS buffer layer, Prog. Photovolt. **26**, 171 (2018).

[79] J. Nishinaga, T. Koida, S. Ishizuka, Y. Kamikawa, H. Takahashi, M. Iioka, H. Higuchi, Y. Ueno, H. Shibata, and S. Niki, Effects of long-term heat-light soaking on $Cu(In, Ga)Se_2$ solar cells with KF post-deposition treatment, Appl. Phys. Express **10**, 092301 (2017).

[80] S. Ishizuka, J. Nishinaga, M. Iioka, H. Higuchi, Y. Kamikawa, T. Koida, H. Shibata, and P. Fons, Si-doped $Cu(In, Ga)Se_2$ photovoltaic devices with energy conversion efficiencies exceeding 16.5% without a buffer layer, Adv. Energy Mater. **8**, 1702391 (2018).

[81] I. L. Eisgruber, J. E. Granata, J. R. Sites, J. Hou, and J. Kessler, Blue-photon modification of nonstandard diode barrier in $CuInSe_2$ solar cells, Sol. Energy Mater. Sol. Cells **53**, 367 (1998).

[82] M. Nichterwitz, R. Caballero, C. A. Kaufmann, H.-W. Schock, and T. Unold, Generation-dependent charge carrier transport in $Cu(In, Ga)Se_2/CdS/ZnO$ thin-film solar-cells, J. Appl. Phys. **113**, 044515 (2013).

[83] S. Dinakaran, S. R. Meher, and G. Cynthia Jemima Swarnavalli, One-dimensional modeling for an investigation into parameter optimization, crossover and red-kink behavior of ZnMgO buffer layer Cd-free $Cu(In, Ga)Se_2$ solar cell, Appl. Phys. A **125**, 399 (2019).

[84] T. P. Weiss, S. Nishiwaki, B. Bissig, R. Carron, E. Avancini, J. Löckinger, S. Buecheler, and A. N. Tiwari, Injection current barrier formation for RbF postdeposition-treated $Cu(In, Ga)Se_2$-based solar cells, Adv. Mater. Interfaces **5**, 1701007 (2018).

[85] J. Keller, F. Chalvet, J. Joel, A. Aijaz, T. Kubart, L. Riekehr, M. Edoff, L. Stolt, and T. Törndahl, Effect of KF absorber treatment on the functionality of different transparent conductive oxide layers in CIGSe solar cells, Prog. Photovolt. **26**, 13 (2018).

[86] T.-Y. Lin, I. Khatri, J. Matsuura, K. Shudo, W.-C. Huang, M. Sugiyama, C.-H. Lai, and T. Nakada, Alkali-induced grain boundary reconstruction on $Cu(In, Ga)Se_2$ thin film solar cells using cesium fluoride post deposition treatment, Nano Energy **68**, 104299 (2020).

[87] F. Q. Huang, B. Deng, D. E. Ellis, and J. A. Ibers, Preparation, structures, and band gaps of $RbInS_2$ and $RbInSe_2$, J. Solid State Chem. **178**, 2128 (2005).

[88] M. Malitckaya, H.-P. Komsa, V. Havu, and M. J. Puska, Effect of alkali metal atom doping on the $CuInSe_2$-based solar cell absorber, J. Phys. Chem. C **121**, 15516 (2017).

[89] M. Nishitani, T. Negami, M. Terauchi, and T. Hirao, Preparation and characterization of $CuInSe_2$ thin films by molecular-beam deposition method, Jpn. J. Appl. Phys. **31**, 192 (1992).

[90] J.-H. Yoon, J.-H. Kim, W. M. Kim, J.-K. Park, Y.-J. Baik, T.-Y. Seong, and J.-h. Jeong, Electrical properties of CIGS/Mo junctions as a function of $MoSe_2$ orientation and Na doping, Prog. Photovolt. **22**, 90 (2014).

[91] R. Caballero, M. Nichterwitz, A. Steigert, A. Eicke, I. Lauermann, H. W. Schock, and C. A. Kaufmann, Impact of Na on $MoSe_2$ formation at the CIGSe/Mo interface in thin-film solar cells on polyimide foil at low process temperatures, Acta Mater. **63**, 54 (2014).

[92] J. Chantana, T. Kato, H. Sugimoto, and T. Minemoto, Enhancement of photovoltaic performances of $Cu(In, Ga)(S, Se)_2$ solar cell through combination of heat-light soaking and light soaking processes, Prog. Photovolt. **26**, 868 (2018).

[93] M. J. Romero, H. Du, G. Teeter, Y. Yan, and M. M. Al-Jassim, Comparative study of the luminescence and intrinsic point defects in the kesterite Cu_2ZnSnS_4 and chalcopyrite $Cu(In, Ga)Se_2$ thin films used in photovoltaic applications, Phys. Rev. B **84**, 165325 (2011).